

REPORT DOCUMENTATION PAGE				Form Approved OMB No. 0704-0188	
Public reporting burden for this collection of information is estimated to average 1 hour per response, including the time for reviewing instructions, searching existing data sources, gathering and maintaining the data needed, and completing and reviewing this collection of information. Send comments regarding this burden estimate or any other aspect of this collection of information, including suggestions for reducing this burden to Department of Defense, Washington Headquarters Services, Directorate for Information Operations and Reports (0704-0188), 1215 Jefferson Davis Highway, Suite 1204, Arlington, VA 22202-4302. Respondents should be aware that notwithstanding any other provision of law, no person shall be subject to any penalty for failing to comply with a collection of information if it does not display a currently valid OMB control number. PLEASE DO NOT RETURN YOUR FORM TO THE ABOVE ADDRESS.					
1. REPORT DATE (DD-MM-YYYY) 01-09-2008		2. REPORT TYPE Annual Report		3. DATES COVERED (From - To) September 1 2007 – August 31 2008	
4. TITLE AND SUBTITLE				5a. CONTRACT NUMBER FA9550-06-1-0056	
				5b. GRANT NUMBER	
				5c. PROGRAM ELEMENT NUMBER	
6. AUTHOR(S) Suresh Menon and Franklin Genin				5d. PROJECT NUMBER	
				5e. TASK NUMBER	
				5f. WORK UNIT NUMBER	
7. PERFORMING ORGANIZATION NAME(S) AND ADDRESS(ES) School of Aerospace Engineering Georgia Institute of Technology Atlanta, GA 30332				8. PERFORMING ORGANIZATION REPORT NUMBER CCL-TR-2008-09-1	
9. SPONSORING / MONITORING AGENCY NAME(S) AND ADDRESS(ES) Computational Mathematics AFOSR 4015 Wilson Blvd, Arlington, VA 22203				10. SPONSOR/MONITOR'S ACRONYM(S) AFOSR/NM	
				11. SPONSOR/MONITOR'S REPORT NUMBER(S)	
12. DISTRIBUTION / AVAILABILITY STATEMENT Unlimited, Unclassified					
13. SUPPLEMENTARY NOTES					
14. ABSTRACT Simulation of multi-phase, turbulent reacting flow is in itself a very complex task but when such flows occur in the presence of strong, unsteady shocks additional complexity can arise. Shock interactions with shear turbulence can change turbulent structures and shock induced heating can trigger ignition, combustion and turbulent flame propagation. In this research, a new and an efficient large-eddy simulation (LES) strategy has been developed to investigate turbulent flows in a high-speed, compressible environment. A new numerical algorithm has been validated that permits a proper capture of strong shocks and shear turbulence simultaneously. This algorithm has been combined with a new dynamic subgrid closure for LES of highly compressible flows such that there are no ad hoc adjustable parameters. Extensive validation has been conducted and application of the hybrid solver to shock-shear interactions, re-shocked Richtmyer-Meshkov instability, and regular and irregular detonations have been demonstrated. These results establish a new capability to simulate high Reynolds number complex flows containing strong shocks, shear turbulence and reacting flows in a multi-phase (gas-liquid-solid) environment.					
15. SUBJECT TERMS Large Eddy Simulation, hybrid shock capturing, detonation, shock-shear interactions, Richtmyer-Meshkov instability					
16. SECURITY CLASSIFICATION OF:			17. LIMITATION OF ABSTRACT UU	18. NUMBER OF PAGES 52	19a. NAME OF RESPONSIBLE PERSON Suresh Menon
a. REPORT Unclassified	b. ABSTRACT Unclassified	c. THIS PAGE Unclassified			19b. TELEPHONE NUMBER (include area code) 404-894-9126

Personnel Supported During Duration of Grant

Franklin M. Genin (100%)	Graduate Student, Georgia Institute of Technology, Atlanta
Kalyana Gottiparthi (25%)	Graduate Student, Georgia Institute of Technology, Atlanta
Satoshi Ukai (25%)	Graduate Student, Georgia Institute of Technology, Atlanta
Srikant Srinivasan (15%)	Research Engineer, Georgia Inst. of Technology, Atlanta
Suresh Menon	Professor, Georgia Institute of Technology, Atlanta

Publications

1. Fryxell, B. and Menon, S., ``Simulation of Richtmyer-Meshkov Instability," to appear in *Physica Scripta*, 2008.
2. F. Genin and S. Menon, "Simulation of Interaction of Shocks with Turbulent Shear Layers Using Large-Eddy Simulations", *under preparation for Computer and Fluids*
3. F. Génin and S. Menon, "Simulation of Turbulent Mixing behind a Strut Injector in Supersonic Flow", invited paper, AIAA-2009-0132, accepted for presentation at the *47th AIAA Aerospace Sciences Meeting*.
4. S. Ukai, F. Génin, S. Srinivasan and S. Menon, "Large Eddy Simulation of Re-shocked Richtmyer-Meshkov Instability" AIAA-2009-0944, accepted for presentation at the *47th AIAA Aerospace Sciences Meeting*.
5. K. Gottiparthi, F. Génin, S. Srinivasan and S. Menon, "Simulation of Cellular Detonation Structures in ethylene-Oxygen Mixtures" AIAA-2009-0437, accepted for presentation at the *47th AIAA Aerospace Sciences Meeting*.

AFRL Point of Contact

Dr. Douglas Nance, AFRL/MNAC, Eglin AFB, FL, Phone (850) 883-2684. Regular bi-monthly meetings at Georgia Institute of Technology.

Discoveries, inventions, patents

None

Awards

None

Transitions

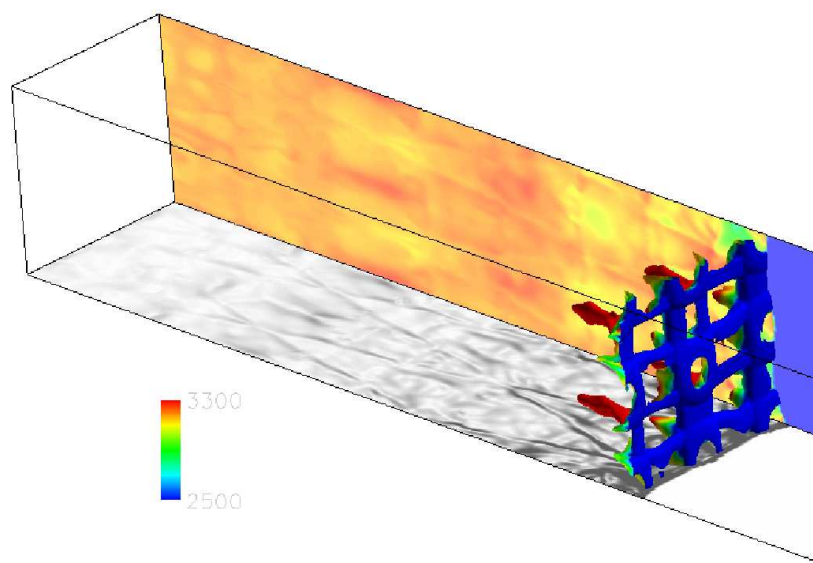
The code developed and described here has been delivered to AFRL/MNAC for their in-house classified studies of the Agent Defeat problems. Successful application of these codes to practical problems has been demonstrated at Eglin AFB. Classified reports have been submitted by Eglin AFB to AFOSR.

CCL Report 2008-09-1

Simulation of Compressible Multi-Phase Turbulent Reacting Flows

Suresh Menon and Franklin Génin

Computational Combustion Laboratory
School of Aerospace Engineering
Georgia Institute of Technology
270 Ferst Drive
Atlanta, Georgia 30332-0150
<http://www.ccl.gatech.edu>



Sponsored by: *Air Force Office of Scientific Research*
Contract Number: *FA9550-06-1-0056*
Date: *September 1, 2008*

TABLE OF CONTENTS

LIST OF TABLES	ii
LIST OF FIGURES	iii
SUMMARY	iv
I INTRODUCTION	1
II SUMMARY OF RESULTS	3
2.1 New Hybrid Framework for Shock-Turbulence-Flame Interactions . .	5
2.2 New Sub-Grid Closure for Compressible Turbulent Flows	6
III FORMULATION AND ALGORITHMS	8
3.1 Governing equations	8
3.1.1 Filtered Navier-Stokes Equations	8
3.1.2 Subgrid Closure Model	10
3.1.3 Localized dynamic closure for subgrid model coefficients . . .	11
3.1.4 Realizability conditions	14
3.2 Hybrid Algorithm for Shock-Shear Simulation	14
3.2.1 Description of the flux-difference splitting scheme	15
3.2.2 Validation of the flux-difference splitting scheme	17
3.2.3 Validation of the LES methodology	18
IV RESULTS AND DISCUSSION	24
4.1 Richtmyer-Meshkov Instability	24
4.2 Regular and Irregular Cellular Detonations	27
4.3 Shock-Shear Interactions in a Scramjet	29
V CONCLUSIONS AND FUTURE PLANS	33
APPENDIX A — HLLC AND HLLC RIEMANN SOLVERS	39

LIST OF TABLES

4.1	Grid resolution and domain size for various test cases	25
4.2	Resolution for regular and irregular detonation simulations.	28

LIST OF FIGURES

3.1	Density profile for two outwards-going infinite strength shocks.	17
3.2	Sedov's point explosion pressure profiles.	18
3.3	Carbuncle test case using contact-preserving and mixed Riemann Solvers	19
3.4	Evolution of the density for the Shu-Osher problem. —, Hybrid (N=200)- - -, pure upwind (N=200) ⋯, Hybrid (N=400) ⋄, pure upwind (N=400) ○	20
3.5	Simulations of multi-mode Richtmyer-Meshkov instabilities using hybrid PPM/4 th (top) and hybrid HLLCE/4 th (bottom): Temperature fields (left) and switch fields (right).	21
3.6	Computational set-up	22
3.7	Shock-Turbulence interaction for a Mach number of 1.29	22
4.1	Geometry of the Simulation	24
4.2	Mixing length before reshock	25
4.3	Overall mixing length growth	25
4.4	Iso-surface of total vorticity magnitude, colored by mass ratio of air .	26
4.5	2D Spectra of the x-component of velocity	27
4.6	Numerical soot foil recording maximum pressure showing regular cellular structures from the current simulation (left) and from Deiterding [14] (right).	28
4.7	Numerical soot foil (left) and instantaneous field of density gradient (right) for an irregular detonation (case II)	29
4.8	30
4.9	Mixing Layer configuration, no shock	31
4.10	Q-criterion visualization	31
4.11	Mixing Layer growth rate	32
A.1	Two characteristic waves, and their characteristic wavespeeds.	40
A.2	Three characteristic waves, and their characteristic wavespeeds.	42

SUMMARY

Simulation of multi-phase, turbulent reacting flow is in itself a very complex task but when such flows occur in the presence of strong, unsteady shocks additional complexity can arise. Shock interactions with shear turbulence can change turbulent structures and shock induced heating can trigger ignition, combustion and turbulent flame propagation. There are many practical applications of interest to US Air Force, such as scramjets, pulse detonation engines, multi-phase detonation (explosives containing inert or reactive particles), and detonation interaction with reactive mixtures where multi-phase (gas-liquid, gas-solid) physics couple with shock-turbulence-flame interactions. Simulation of such flows (either using direct or large-eddy simulation approach) requires a numerical strategy that can simultaneously capture strong shock motion and turbulence-flame interactions occurring over a wide range of spatial and temporal scales. In this research, a new and an efficient large-eddy simulation (LES) strategy has been developed to investigate turbulent flows in a high-speed, compressible environment. A new numerical algorithm has been developed that permits a proper capture of the discontinuities that arise at supersonic speeds using a hybrid Riemann solver that shows reduced sensitivity to classical solver instabilities. Since an upwind shock-capturing schemes can dissipate turbulent features the current hybrid approach uses a low dissipation algorithm in regions of high shear without shocks. In order to simulate high Reynolds number flows, large-eddy simulation (LES) using a new compressible subgrid closure has been developed and validated. Direct simulations of shock/turbulence interactions for Mach numbers ranging from 1.29 to 3.0 have been used to identify the most important terms in the closure strategy adopted for shock-containing flows. The models for these terms and the dynamic evaluation of the closure coefficients as a part of the solution demonstrated in this study lead to a very general methodology with no *ad hoc* constants. This closure model has been validated by performing Large Eddy Simulations of the shock / turbulence flow configurations as well of other flow configurations, such as Richtmyer-Meshkov instabilities, regular and irregular gaseous detonations, and mixing-augmentation configurations based on shock / turbulent shear interactions.

CHAPTER I

INTRODUCTION

A class of problems of both great fundamental interest and practical relevance is in the field of highly compressible turbulent flows of multi-fluids. Typical challenging problems are in multi-phase detonations (these can involve gaseous detonation wave interacting with two-phase reactive mixture or detonation products containing reactive or inert particles), and in strong shock wave propagation in turbulent media followed by shock induced ignition and combustion. Shock interaction with turbulence and/or flames have many practical applications for US Air Force in applications such as scramjets, pulse-detonation engines (PDE), stage separation, supersonic cavity oscillations, hypersonic aerodynamics, detonation induced structural destruction, detonation induced destruction of chemical and biological agents, etc.

In shock-turbulence interactions, post-shock and/or post-detonation turbulence evolution is of particular interest from a fundamental perspective as well since some of the turbulent physics may not follow conventional well known scaling laws. For example, extensive studies of Richtmyer-Meshkov instability (RMI) are currently underway, both experimentally [55, 2, 9] and numerically [11, 28, 49] since RMI is a fundamental instability that occurs when a passing shock wave interacts with a perturbed density interface separating gases of different densities [5, 57]. Vorticity generation occurs around the interface and during subsequent evolution develops into many scales of turbulent like structures. If this turbulent field is re-shocked, additional scales of turbulence have been shown to be generated. RMI and reshocked-RMI [59, 60, 49] are very relevant for core-collapse supernova dynamics, but can also occur in the detonation scenarios involving reacting flows, including supersonic combustion ramjets (SCRAMJETS) and pulse detonation engines. Shock induced mixing changes associated with RMI and re-shocked RMI are therefore, of considerable interest from practical point of view. There are also other fundamental unresolved issues regarding RMI. For example, recent studies in re-shocked RMI suggest that the scales of turbulence in the post shock region may not strictly follow the classical Kolmogorov $-5/3$ inertial range scaling [59, 44]. If so, then this type of turbulence may require different scaling arguments, and hence new types of subgrid closure(s).

There is very little experimental data (even when available the data is sparse and not time-resolved) and these multi-physics problems are also inherently difficult to solve due to the very large range of temporal and spatial scales involved. Numerical approach must capture strong moving shocks and fine-scales of turbulence. Conventional shock capturing schemes are too dissipative for this purpose. As a result, new high-order schemes, such as the ninth-order weighted essentially non-oscillatory (WENO) shock-capturing schemes have been developed for direct numerical simulations (DNS). Most of the past RMI simulations (primarily using DNS) using such schemes have been restricted to 2D [23, 49, 33] and only a few studies have reported

using full 3D DNS or LES approaches [11, 28]. Furthermore, all these studies are in very simplified (planar) shock-tube type geometries. However, for practical application to SCRAMJET or PDE type applications, the geometrical complexities and test conditions are such that DNS and even very high order schemes are not computationally practical. On the other hand, large-eddy simulation (LES) may be a viable alternative since it has already shown potential for subsonic problems [31, 41]. However, in order to conduct LES of supersonic and shock-dominated flows new algorithms and subgrid closures for highly compressible flow have to be developed and validated. LES studies of compressible mixing, shock-shear interactions, detonations and RMI have just started to appear [28, 22, 25, 24] but there are still many issues to be addressed. For example, in addition to the scales associated with the shock structure and fine-scale turbulence, particle (e.g., liquid droplets) motion, fuel-air mixing and finite-rate reactions have to be included for some applications. Chemical kinetics are usually very stiff requiring very small time-steps to properly resolve turbulence-chemistry-shock interactions. Implicit schemes have only limited functionality (since there is a limit beyond which the time scales of interactions have to be resolved), and also have problems scaling in massively parallel systems.

Thus, there are still many challenges to study of shock-turbulence-flame (STF) interaction in both canonical and practical systems. Some of these challenges have been addressed over the last few years at Georgia Tech, and has resulted in a new multi-scale, multi-phase solver that can simulate STF interactions with good accuracy. This capability was developed in part using support from AFOSR and the code has been delivered to Eglin AFB to support their in-house (classified) applications. In fact, the applications of this code in Eglin AFB to problems of AF practical interest demonstrates our ability to transition from fundamental studies conducted in GT to more complex practical problems of AF interest.

This report summarized the key results obtained in the last fiscal year of this research effort. Since this is also its final year, some key issues and developments reported in previous reports have been included for completeness. Further results and analysis are reported in cited publications.

CHAPTER II

SUMMARY OF RESULTS

To establish a validated simulation capability for STF interaction studies, we leverage a code called LESLIE3D (Large-Eddy Simulation using LInear Eddy in 3D), originally developed to study turbulent two-phase combustion in subsonic flows as in gas turbine and ramjet combustors. This code is a multi-block, structured grid solver of the fully compressible Navier-Stokes equations using a finite-volume scheme that is second-order accurate in time and up to fourth-order accurate in space. In addition to LES the code can be used to perform DNS and has been extensively validated in many non-reacting and reacting flow applications(see [41] and other cited references). To extend this code to handle shock and detonation physics two key challenges have been continuously addressed and successfully resolved in the current effort. The first challenge consists in developing a numerical approach that adapts locally to the unsteady shock motion and/or compressive regions without contaminating or dissipating the turbulent and/or flame structures. This requires developing and validating a new hybrid approach within the generalized multi-block approach that can achieve simultaneously, very low dissipation in smooth flow regions and proper shock capturing in the regions of high compressibility. The second challenge is to develop improved LES sub-grid closure model to include the effects of high compressibility on the turbulence evolution. A new localized dynamic sub-grid closure that can handle some of the underlying physics of STF interactions has been developed and validated.

In the following, we briefly summarize the key progress and success of the effort conducted over the last 3 years. Some of these results and application of the solver have been reported in publications and more detailed papers are currently being written. Here, we list the publications past and planned for completeness:

Papers directly related to research under the current AFOSR project:

1. Fryxell, B. and Menon, S., "Hybrid Simulations of Richtmyer-Meshkov Instability," AIAA-2005-0314, 43rd AIAA Aerospace Sciences Meeting, Reno, NV, January, 2005.
2. Génin, F., Fryxell, B., and Menon, S., "Simulation of Detonation Propagation in Turbulent Gas-Solid Reactive Mixtures," AIAA-2005-3967, 41st AIAA/ASME/ASEE Joint Propulsion Conference, Tucson, AZ, July 11-14, 2005.
3. Génin F., Fryxell, B. and Menon, S., "Hybrid Large-Eddy Simulation of Detonation in Reactive Mixtures," 20th International Conference on Detonations, Explosions and Shock Waves, Montreal CA, August 1-4, 2005.
4. Menon, S., "A Multi-Scale Simulation Methodology for Compressible Flows and Turbulent Combustion" Proceedings of the Third European Combustion Meeting, ECM2007, Chania, Crete, April 11-13, 2007.

5. Fryxell, B. and Menon, S., “Simulation of Richtmyer-Meshkov Instability,” to appear in *Physica Scripta*, 2008.
6. Génin, F. and Menon, S., “Simulation of Interaction of Shocks with Turbulent Shear Layers Using Large-Eddy Simulations,” *Computer and Fluids*, 2008 (to be submitted).
7. Génin, F. and Menon, S., “Simulation of Turbulent Mixing Behind a Strut Injector in Supersonic Flow,” invited paper, AIAA-2009-0132, 47th AIAA Aerospace Sciences Meeting, January 2009.
8. Ukai, S., Génin, F., Srinivasan, S. and Menon, S., “Large-Eddy Simulation of Re-shocked Richtmyer-Meshkov Instability,” AIAA-2009-0944, 47th AIAA Aerospace Sciences Conference, January 2009.
9. Gottiparthi, K., Génin, F., Srinivasan, S. and Menon, S., “Simulation of Cellular Detonation Structures in Ethylene-Air Mixtures,” AIAA-2009-0437, 47th AIAA Aerospace Sciences Conference, January 2009.

Transition of the numerical and subgrid algorithms developed in this research to other research is a key demonstration of the validity and the relevance of the new approaches. In this regard, we have been very successful with many publications (for research funded by ONR, DTRA, AFOSR and NASA) that employed the algorithms developed under the current AFOSR project. Papers that uses the hybrid solver developed under the AFOSR project:

1. Miki, K. and Menon, S., “Local Dynamic Subgrid Closure for Compressible MHD Turbulence Simulation,” AIAA-2006-2891, 37th AIAA Plasma-dynamics and Lasers Conference, San Francisco, CA, 5-8 June 2006.
2. Schulz, J., Miki, K., and Menon, S., “Simulation of MHD Turbulence-Chemistry Interaction in Supersonic Flow,” AIAA Paper 2006-2894, 36th AIAA Plasma-dynamics and Lasers Conf., San Francisco, 5-8 June, 2006.
3. Miki, K., Schulz, J. and Menon, S., “Large-Eddy Simulation of Supersonic Plasma Flow over a Backward Facing Step,” *Proceedings of the Fifth Turbulent Shear Flow Phenomenon (TSFP-5)*, pp. 985-990, 2007.
4. Balakrishanan, K. and Menon, S., “Simulation of Detonation Propagation Through Solid Particle Clouds and Subsequent Dispersion of Particles,” AIAA-2008-4689, 44th AIAA Joint Propulsion Conference, Hartford, CT, July 21-23, 2008.
5. Balakrishanan, K., Génin, F., Menon, S., and Nance, D., “Numerical Study of Shock Overpressure and Propagation Characteristics from Detonations in Homogeneous Explosives Nitromethane, HMX, and TNT,” 2008 (under preparation).

6. Balakrishanan, K., Génin, F., Menon, S., and Nance, D., “Numerical Study of Shock Overpressure and Particle Motion from Detonations in Heterogeneous Explosives containing Dense Inert Particles,” 2008 (under preparation).
7. Miki, K., Schulz, J. and Menon, S., “Large-Eddy Simulation of Non-Equilibrium Plasma-Assisted Combustion in Supersonic Flow,” AIAA-2008-5072, 44th AIAA Joint Propulsion Conference, Hartford, CT, July 21-23, 2008.
8. Miki, K., Schulz, J. and Menon, S., “Large-Eddy Simulation of Equilibrium Plasma-Assisted Combustion in Supersonic Flow,” *Proceedings of the Combustion Institute*, Vol. 32, 2008 (to appear).
9. Miki, K., and Menon, S., “Localized Dynamic Subgrid Closure for Simulation of Magnetohydrodynamics Turbulence,” *Physics of Plasma*, Vol. 15, 072306, 2008.

2.1 New Hybrid Framework for Shock-Turbulence-Flame Interactions

A major problem for DNS and LES using algorithms developed for smooth flows is that they produce unphysical oscillations in regions containing shocks and contact discontinuities, and require very refine resolution in the discontinuity region [34]. On the other hand, shock-capturing schemes have not shown potential for resolving unsteady shear flows in conjunction with shock waves, unless the resolution is high enough so that the dissipation necessary to stabilize discontinuities in typical shock-capturing schemes do not produce an unphysical rate of decay of turbulent features.

In order to capture strong unsteady shock motion and also the important scales of turbulence, two key capabilities were developed and validated. For shock capturing we initially (2005-2006) implemented Piecewise Parabolized Method (PPM), which is nominally $O(3)$ away from shocks but is limited to uniform or weakly stretching Cartesian grids. In order to simulate shocks in more complex flows, we developed an alternate high-order flux difference splitting method in 2006-2007 within the framework of our multi-block structured flow solver. A Riemann problem is constructed at the interface separating two cells, using high-order MUSCL type interpolation (with a Monotonized Central limiter to prevent non-monotonic behavior) and solved using an adaptive approximate Riemann solver. This adaptive approximate Riemann solver is based on the Harten-Lax-Leer (*HLL*) family of Riemann solvers [27]. In particular, we combine the contact preserving *HLLC* with a non-contact preserving *HLLE* in order to avoid parasitic oscillation in the post shock regions. Detailed validation of this combined *HLLC/E* approach has been conducted and demonstrated its capability to achieve proper shock and discontinuity capturing with minimal instabilities. Switching between *HLLC* and *HLLE* is based on local sensors that requires no ad hoc adjustment from the user. This sensor uses both pressure ratio and velocity divergence. The resulting hybrid Riemann solver differs from earlier hybrid solvers [45, 46] in the sense that, instead of applying *HLLE* everywhere in the shock

thickness, HLLC/E uses HLLE only in the direction transverse to the detected shock. This limits the instabilities in the shock region and also limits the amount of extra dissipation introduced by HLLE. As shown in our studies this sensor is very robust, thanks to the uniqueness of the shock characteristics and has required no ad hoc user input.

The overall accuracy of the HLLC/E is second order, although viscous terms are still computed using fourth order accuracy. The HLLC/E model is implemented within our full 3D generalized multi-block, multi-phase solvers LESLIE3D and therefore, it can exploit all the in-built capabilities of the code.

To simulate STF interactions, another type of hybrid approach is developed, whereby, the $O(4)$ smooth flow solver in LESLIE3D is used in regions with no shocks, and the HLLC/E approach is used in regions of strong discontinuities. The switch [22] employs detecting both pressure and density gradients and has been successfully applied to practical turbulent problems [25, 24]. The regions of strong discontinuities are detected by a measure of the smoothness of the solution locally so that the switching between the two schemes is natural, and again requires no user input.

Thus, we now have a baseline generalized solver that employs two layers of hybrid, locally adapting algorithms: (a) a shock capturing scheme switching to $O(4)$ smooth flow solvers away from regions of strong discontinuities, and (b) within the regions of strong discontinuities a switch between contact discontinuity preserving (HLLC) and non-contact preserving (HLLE) so that both shocks and contact discontinuities are captured in full 3D with minimal instabilities. Application to many canonical and complex flows have demonstrated the ability of this new solver. Results for some of the validation studies are presented later.

2.2 New Sub-Grid Closure for Compressible Turbulent Flows

The method described above is used to solve the Navier-Stokes equations in general but in highly turbulent flows, the grid resolution is insufficient to do direct numerical simulation (DNS) and therefore, we have to resort to large-eddy simulations (LES). LES capability in LESLIE3D for subsonic reacting flows is well established and is based on a localized dynamic closure for the sub-grid turbulent kinetic energy (LDKM). The LDKM approach allows the model coefficients to evolve as a part of the solution, and thus, there are no model constants to adjust. This provides a generality critical to study complex flows.

To extend to highly compressible flows, additional sub-grid terms (that are typically ignored in low-speed flows) have to be re-assessed. For example, the sub-grid enthalpy flux is typically modeled using the sub-grid eddy viscosity and a constant turbulent Prandtl number in low speed flows. However, in compressible flow, the constant Prandtl number assumption is not accurate and therefore, a new scale-similarity dynamic closure for the turbulent Prandtl number has been developed. In addition, the diffusion of k^{sgs} due to pressure fluctuations, which plays an important role during the interaction of a turbulent field with a shock, has the same structural form as the

diffusion of energy due to the subgrid energy fluctuations. In a perfect gas these two unclosed terms are proportional, and therefore, a model for this term is also achieved through the dynamic computation of the turbulent Prandtl number.

Finally, the evolution of the turbulent kinetic energy in compressible flows is dependent on the pressure-dilatation correlation. This physical phenomenon transfers energy between internal and kinetic energy, and can be either a source or a sink of kinetic energy. An earlier analytical study [47] showed that the pressure-dilatation correlation becomes important in non-equilibrium flows, that is, when production and dissipation of turbulent kinetic energy are significantly unbalanced. A dependence on the square of the turbulent Mach number is also derived from this work and used in the current closure.

In summary, the sub-grid closure for compressible flow now employs additional dynamic closure for the turbulent Prandtl number, the kinetic energy diffusion due to pressure fluctuations and the pressure-dilatation correlation.

The developments described here have also permitted high-fidelity simulations of detonation processes. This combustion regime consists in a high-speed shock traveling in a low-temperature reactive mixture. The gas is compressed and heated through the compression, and auto-ignition is achieved. The heat released by the reaction *feeds* back the main wave. A good capture of the phenomenon requires a proper capture of the running shock, an accurate treatment of the chemical source terms, and a low dissipation in the post-shock region, in order to capture the turbulent structures emanating from the triple points on the detonation front. These capabilities have been developed and validated in our solver.

In the following chapters we discuss the key results of this study.

CHAPTER III

FORMULATION AND ALGORITHMS

3.1 Governing equations

3.1.1 Filtered Navier-Stokes Equations

The direct resolution of the Navier-Stokes equations requires an increasingly high computational expense as the flow Reynolds number is increased. Except for a few canonical flows, this method cannot be adopted for the simulation of practical flows, and so LES with appropriate subgrid closure is a viable option. The compressible LES equations are obtained by spatially filtering the Navier-Stokes equations using a top-hat filter (see, *e.g.* [56]), appropriate for finite volume schemes. If we define \bar{f} as the spatially filtered variable f , and \tilde{f} as the Favré-filtered variable f , defined by $\tilde{f} = \bar{\rho}f/\bar{\rho}$, where ρ represents the local fluid density, then the LES equations for mass, momentum, total energy and species conservation can be written as:

$$\frac{\partial \bar{\rho}}{\partial t} + \frac{\partial \bar{\rho} \tilde{u}_i}{\partial x_i} = 0 \quad (3.1)$$

$$\frac{\partial \bar{\rho} \tilde{u}_i}{\partial t} + \frac{\partial}{\partial x_j} [\bar{\rho} \tilde{u}_i \tilde{u}_j + \bar{P} \delta_{ij} - \bar{\tau}_{ij} + \tau_{ij}^{sgs}] = 0 \quad (3.2)$$

$$\frac{\partial \bar{\rho} \tilde{E}}{\partial t} + \frac{\partial}{\partial x_i} \left[(\bar{\rho} \tilde{E} + \bar{P}) \tilde{u}_i + \bar{q}_i - \tilde{u}_j \bar{\tau}_{ij} + H_i^{sgs} + \sigma_i^{sgs} \right] = 0 \quad (3.3)$$

$$\frac{\partial \bar{\rho} \tilde{Y}_k}{\partial t} + \frac{\partial}{\partial x_i} \left[\bar{\rho} (\tilde{Y}_k \tilde{u}_i + \tilde{Y}_k \tilde{V}_{i,k}) + Y_{i,k}^{sgs} + \theta_{i,k}^{sgs} \right] = 0 \quad k = 1, \dots, N_s \quad (3.4)$$

Here, ρ is the density, $(u_i)_{i=1,2,3}$ is the velocity vector in Cartesian coordinates, P is the pressure, T is the temperature, and Y_k is the k -th species mass fraction. Also, N_s is the total number of species. The total energy of the system is the sum of the internal energy e and the kinetic energy. As a consequence, the filtered total energy is the sum of the filtered internal energy \tilde{e} , the resolved kinetic energy, $(1/2)[\tilde{u}_i \tilde{u}_i]$ and the resolved subgrid kinetic energy (k^{sgs}), given by $k^{sgs} = (1/2)[\bar{u}_i \bar{u}_i - \tilde{u}_i \tilde{u}_i]$. A perfect gas equation of state is assumed here and neglecting the correlation between subgrid species and the subgrid temperature fluctuations, the equation of state reads:

$$\bar{P} = \bar{\rho} \tilde{R} \tilde{T} \quad (3.5)$$

The filtered internal energy per unit mass is then:

$$\tilde{e} = \sum_{k=1, \dots, N_s} \tilde{Y}_k \int_0^{\tilde{T}} c_{v,k}(T) dT \quad (3.6)$$

where the mixture gas constant \tilde{R} is obtained using the specie molecular weights $(MW_k)_{k=1,\dots,NS}$ and R_u the universal gas constant, as:

$$\tilde{R} = \sum_{k=1,\dots,NS} \tilde{Y}_k \frac{R_u}{MW_k} \quad (3.7)$$

The filtered static enthalpy per unit mass \tilde{h} is defined as $\tilde{\rho}\tilde{h} = \tilde{\rho}\tilde{e} + \tilde{P}$ and for perfect gas can be expressed as:

$$\tilde{h} = \sum_{k=1,\dots,NS} \tilde{Y}_k \int_0^{\tilde{T}} c_{p,k}(T) dT \quad (3.8)$$

where $c_{p,k} = c_{v,k} + R_k$. The specific heat at constant pressure k -th species k , $c_{p,k}$ are all obtained from classical temperature curve-fits [26] as polynomials of order 4:

$$c_{p,k}(T) = \sum_{i=0,\dots,4} a_{k,i} T^i \quad (3.9)$$

$$h_k(T) = \int_0^T c_{p,k}(T) dT = \sum_{i=1,\dots,5} \frac{a_{k,i-1}}{i} T^i \quad (3.10)$$

The filtered viscous stress tensor, $\overline{\tau_{ij}}$, and the filtered heat-flux vector, $\overline{q_i}$ are approximated as:

$$\overline{\tau_{ij}} = 2\mu(\tilde{T}) \left(\tilde{S}_{ij} - \frac{1}{3} \tilde{S}_{kk} \delta_{ij} \right) \quad (3.11)$$

$$\overline{q_i} = -\kappa(\tilde{T}) \frac{\partial \tilde{T}}{\partial x_i} + \tilde{\rho} \sum_{k=1,\dots,NS} \tilde{h}_k \tilde{Y}_k \tilde{V}_{i,k} \quad (3.12)$$

In the previous expression, S_{ij} represents the rate of strain, given as:

$$\tilde{S}_{ij} = \frac{1}{2} \left(\frac{\partial \tilde{u}_i}{\partial x_j} + \frac{\partial \tilde{u}_j}{\partial x_i} \right) \quad (3.13)$$

Empirical temperature-dependent laws are used for the evaluation of the viscosity. Following [35], the viscosity is computed using a power-law temperature relation, with an exponent of 0.76 for the case of shock / isotropic turbulence interaction, and a Sutherland law is used for shock / shear interaction problem. In all cases, the thermal conductivity is obtained by assuming a constant Prandtl number ($Pr = c_p \mu / \kappa = 0.72$). Finally, $\tilde{V}_{i,k}$ is the filtered diffusion velocity for k -th species and is modeled using Fick's law:

$$\tilde{V}_{i,k} = \frac{-D_k}{\tilde{Y}_k} \frac{\partial \tilde{Y}_k}{\partial x_i} \quad (3.14)$$

where D_k is the k^{th} -species diffusion coefficient.

All the *subgrid-scale* terms, denoted with a *sgs* superscript require specific modeling to close the above system of LES equations. These terms are defined as:

$$\tau_{ij}^{sgs} = \tilde{\rho} (\tilde{u_i u_j} - \tilde{u_i} \tilde{u_j}) \quad (3.15)$$

$$H_i^{sgs} = \bar{\rho} \left(\widetilde{Eu_i} - \widetilde{E} \widetilde{u_i} \right) + (\overline{u_i P} - \widetilde{u_i} \bar{P}) \quad (3.16)$$

$$\sigma_i^{sgs} = (\overline{u_j \tau_{ij}} - \widetilde{u_j} \overline{\tau_{ij}}) \quad (3.17)$$

$$Y_{i,k}^{sgs} = \bar{\rho} \left(\widetilde{u_i Y_k} - \widetilde{u_i} \widetilde{Y_k} \right) \quad (3.18)$$

The closure strategy to model the terms denoted as subgrid-scale will be presented next.

3.1.2 Subgrid Closure Model

An eddy-viscosity type closure is adopted in this study. The eddy viscosity, ν_t , is evaluated using a characteristic length-scale, provided by the local grid size ($\bar{\Delta}$), and a characteristic subgrid velocity, which is obtained from the subgrid kinetic energy k^{sgs} , so that $\nu_t = c_\nu \bar{\Delta} \sqrt{k^{sgs}}$. The unclosed terms in the momentum equation, the subgrid stresses τ_{ij}^{sgs} are then closed as:

$$\tau_{ij}^{sgs} = -2\bar{\rho}\nu_t \left(\widetilde{S_{ij}} - \frac{1}{3} \widetilde{S_{kk}} \delta_{ij} \right) + \frac{2}{3} k^{sgs} \delta_{ij} \quad (3.19)$$

The two unclosed terms in the energy equation, H_i^{sgs} and σ_i^{sgs} are modeled together following:

$$H_i^{sgs} + \sigma_i^{sgs} = (\bar{\rho}\nu_t + \mu) \frac{\partial k^{sgs}}{\partial x_i} + \frac{\bar{\rho}\nu_t c_p}{Pr_t} \frac{\partial \widetilde{T}}{\partial x_i} + \widetilde{u_j} \tau_{ij}^{sgs} \quad (3.20)$$

The subgrid diffusion of species mass fractions, $Y_{i,k}^{sgs}$ is also modeled using an eddy-diffusivity assumption, as:

$$Y_{i,k}^{sgs} = -\frac{\bar{\rho}\nu_t}{Sc_t} \frac{\partial \widetilde{Y_k}}{\partial x_i} \quad (3.21)$$

Thus, to close the filtered equations of mass, momentum and energy conservation using the above relations the local value of k^{sgs} must be determined. In the present study, a transport model for the subgrid kinetic energy is used. The exact governing equation for k^{sgs} reads:

$$\frac{\partial}{\partial t} \bar{\rho} k^{sgs} + \frac{\partial}{\partial x_i} (\bar{\rho} \widetilde{u_i k^{sgs}}) = \mathcal{D}_{k^{sgs}} + \mathcal{P}_{k^{sgs}} + P_{k^{sgs}} - D_{k^{sgs}} \quad (3.22)$$

where $\mathcal{D}_{k^{sgs}}$ represents the diffusion of k^{sgs} , $\mathcal{P}_{k^{sgs}}$ is the pressure dilatation correlation, and $P_{k^{sgs}}$ and $D_{k^{sgs}}$ are the production and dissipation of k^{sgs} , respectively. Their exact expressions are given by:

$$\mathcal{D}_{k^{sgs}} = -\frac{\partial}{\partial x_i} \left((\bar{\rho} \widetilde{K u_i} - \bar{\rho} \widetilde{K} \widetilde{u_i} - \widetilde{u_j} \tau_{ij}^{sgs}) + (\overline{u_i P} - \widetilde{u_i} \bar{P}) - (\overline{u_j \tau_{ij}} - \widetilde{u_j} \overline{\tau_{ij}}) \right) \quad (3.23)$$

$$\mathcal{P}_{k^{sgs}} = \overline{P \frac{\partial u_i}{\partial x_i}} - \bar{P} \frac{\partial \widetilde{u_i}}{\partial x_i} \quad (3.24)$$

$$P_{k^{sgs}} = -\tau_{ij}^{sgs} \frac{\partial \widetilde{u_j}}{\partial x_i} \quad (3.25)$$

$$D_{k^{sgs}} = \left(\overline{\tau_{ij} \frac{\partial u_i}{\partial x_j}} - \overline{\tau_{ij}} \frac{\partial \tilde{u}_i}{\partial x_j} \right) \quad (3.26)$$

The pressure-dilatation correlation and the diffusion and dissipation of k^{sgs} cannot be already obtained, and require additional modeling. By analogy with the Kolmogorov concept of energy cascade, the dissipation of subgrid kinetic energy is evaluated based on the characteristic length- and velocity- scales as $D_{k^{sgs}} = \bar{\rho} c_\epsilon (k^{sgs})^{3/2} / \bar{\Delta}$. The diffusion due to subgrid fluctuations in kinetic energy, subgrid fluctuations in viscous stress, and subgrid fluctuations in pressure all contribute to the global diffusion of k^{sgs} and each require proper modeling each. The first contribution (often referred to as the triple velocity correlation) and the second are modeled together using a k^{sgs} gradient diffusion approach. The diffusion due to pressure fluctuations is often neglected in incompressible, or low-compressibility. It has, however, been found from direct simulations of shock / turbulence interaction (presented in last year's report) that it plays an important role in the k^{sgs} -evolution in shock-containing flows. This term is now closed using an eddy-viscosity assumption as:

$$\overline{u_i P} - \tilde{u}_i \bar{P} = \bar{\rho} \tilde{R} (\widetilde{u_i T} - \tilde{u}_i \tilde{T}) = - \frac{\bar{\rho} \nu_t \tilde{R}}{\sigma_P} \frac{\partial \tilde{T}}{\partial x_i} \quad (3.27)$$

So that the global model for the diffusion of subgrid kinetic energy reads:

$$\mathcal{D}_{k^{sgs}} = \frac{\partial}{\partial x_i} \left[\left(\frac{\bar{\rho} \nu_t}{\sigma_k} + \mu(\tilde{T}) \right) \frac{\partial k^{sgs}}{\partial x_i} + \frac{\bar{\rho} \nu_t \tilde{R}}{\sigma_P} \frac{\partial \tilde{T}}{\partial x_i} \right] \quad (3.28)$$

The pressure-dilatation correlation has been the focus of many studies in the past, mostly from DNS or fundamental analyses [1, 58, 48, 47]. Many of these models were unfortunately obtained from DNS results with non stable initializations. The analytical formulation of Ristorcelli [47] is performed in the acoustic limit, and is adequate in the limit of small turbulent Mach numbers. From this analysis, it appears that the pressure-dilatation correlation is found to be an *out-of-equilibrium* turbulent phenomenon, i.e., when the turbulent production is not balanced by the turbulent dissipation. The expression obtained by [47] reads:

$$\mathcal{P}_{k^{sgs}} = \alpha_{pd} M_t^{sgs2} \left(\frac{\tilde{S} k^{sgs}}{D_{k^{sgs}}} \right)^2 (P_{k^{sgs}} - D_{k^{sgs}}) \quad (3.29)$$

where M_t^{sgs} is the turbulent Mach number based on the local value of k^{sgs} and the local speed of sound. This term becomes important when the flow is both out of equilibrium and the gradient Mach number ($M_t \tilde{S} k^{sgs} / D_{k^{sgs}}$) is large. We employ this model in our closure as well.

3.1.3 Localized dynamic closure for subgrid model coefficients

The closure terms in the LES and the equation for k^{sgs} have six closure coefficients: $(c_\nu, c_\epsilon, \sigma_k, Pr_t, \alpha_{pd}, Sc_t)$. Nominal values for these coefficients have been proposed

in the past (see, *e.g.* [7, 8]). In the present study, a dynamic evaluation of the coefficients is performed, based on the framework of the Localized Dynamic k^{sgs} Model (LDKM) [32, 30]. This model uses the experimentally observed [38] similarity between subgrid stresses and Leonard stresses to evaluate the closure coefficient from directly computable quantities. The similarity hypothesis implies that the Leonard stress is similar in nature to the subgrid stress. In particular, the trace of these tensors, $\langle \bar{\rho} \rangle k^{test}$ and $\bar{\rho} k^{sgs}$ respectively, are similar.

Noting $\langle f \rangle$ the explicit application of a top-hat filter of size $\hat{\Delta}$ ($\hat{\Delta} > \bar{\Delta}$) performed on variable f , the Leonard stress can be expressed as:

$$\mathcal{L}_{ij} = \langle \bar{\rho} \rangle \left(\frac{\langle \bar{\rho} \tilde{u}_i \tilde{u}_j \rangle}{\langle \bar{\rho} \rangle} - \frac{\langle \bar{\rho} \tilde{u}_i \rangle \langle \bar{\rho} \tilde{u}_j \rangle}{\langle \bar{\rho} \rangle^2} \right) \quad (3.30)$$

In the current closure, the Leonard stress at the test filter level (which is known explicitly is related to the subgrid model at the test filter level by the similarity assumption. Thus, using the test-scale kinetic energy ($k^{test} = 1/2 \mathcal{L}_{ii}$) as:

$$\mathcal{L}_{ij} = -2 \langle \bar{\rho} \rangle c_\nu \sqrt{k^{test}} \hat{\Delta} \left(\frac{\langle \bar{\rho} \tilde{S}_{ij} \rangle}{\langle \bar{\rho} \rangle} - \frac{1}{3} \frac{\langle \bar{\rho} \tilde{S}_{kk} \rangle}{\langle \bar{\rho} \rangle} \delta_{ij} \right) + \frac{2}{3} \langle \bar{\rho} \rangle k^{test} \delta_{ij} \quad (3.31)$$

so that this relation has c_ν as the only remaining unknown. \mathcal{L}_{ij} being a symmetric tensor, equation 3.31 leaves us with five independent relations for the determination of one unknown. The over-determination is circumvented by using a least-square method([36]) so that c_ν is computed as:

$$c_\nu = -\frac{\mathcal{M}_{ij} \mathcal{L}'_{ij}}{2 \mathcal{M}_{ij} \mathcal{M}_{ij}} \quad (3.32)$$

where:

$$\mathcal{M}_{ij} = \sqrt{k^{test}} \langle \bar{\rho} \rangle \hat{\Delta} \left(\frac{\langle \bar{\rho} \tilde{S}_{ij} \rangle}{\langle \bar{\rho} \rangle} - \frac{1}{3} \frac{\langle \bar{\rho} \tilde{S}_{kk} \rangle}{\langle \bar{\rho} \rangle} \delta_{ij} \right) \quad (3.33)$$

$$\mathcal{L}'_{ij} = \mathcal{L}_{ij} - \frac{2}{3} \langle \bar{\rho} \rangle k^{test} \delta_{ij} \quad (3.34)$$

The exact governing equation for k^{test} can be written as:

$$\frac{\partial}{\partial t} \bar{\rho} k^{test} + \frac{\partial}{\partial x_i} (\langle \bar{\rho} \tilde{u}_i \rangle k^{test}) = \mathcal{D}_{k^{test}} + \mathcal{P}_{k^{test}} + P_{k^{test}} - D_{k^{test}} \quad (3.35)$$

where the expression for diffusion, pressure correlation, production and dissipation at the test-scale level are fully expressed as functions of the resolved variables and the subgrid stresses. In particular, the dissipation is given by:

$$D_{k^{test}} = \left\langle (\bar{\tau}_{ij} - \tau_{ij}^{sgs}) \frac{\partial \tilde{u}_j}{\partial x_i} \right\rangle - \langle (\bar{\tau}_{ij} - \tau_{ij}^{sgs}) \rangle \frac{1}{\langle \bar{\rho} \rangle} \left\langle \bar{\rho} \frac{\partial \tilde{u}_j}{\partial x_i} \right\rangle \quad (3.36)$$

Using the similarity assumption, the dissipation of k^{test} can be modeled similar to the model for the dissipation of k^{sgs} , $D_{k^{test}} = \widehat{\rho} c_\epsilon (k^{test})^{3/2} / \widehat{\Delta}$, where again, only the closure coefficient remains unknown. Assuming that the viscosities can be extracted from the filtering operation, the last coefficient, c_ϵ , are expressed as:

$$c_\epsilon = \frac{\widehat{\Delta}}{\langle \bar{\rho} \rangle (k^{test})^{\frac{3}{2}}} \left((\mu + \mu_t) \left[\left\langle \widetilde{\Sigma}_{ij} \frac{\partial \widetilde{u}_j}{\partial x_i} \right\rangle - \left\langle \widetilde{\Sigma}_{ij} \right\rangle \frac{\partial \langle \widetilde{u}_j \rangle}{\partial x_i} \right] - \frac{2}{3} \left[\left\langle \bar{\rho} k^{sgs} \frac{\partial \widetilde{u}_k}{\partial x_k} \right\rangle - \langle \bar{\rho} k^{sgs} \rangle \frac{\partial \langle \widetilde{u}_k \rangle}{\partial x_k} \right] \right) \quad (3.37)$$

where Σ_{ij} is twice the traceless strain tensor:

$$\widetilde{\Sigma}_{ij} = 2 \left(\widetilde{S}_{ij} - \frac{1}{3} \widetilde{S}_{kk} \delta_{ij} \right) \quad (3.38)$$

This expression models both the solenoidal and dilatational dissipation together, using the same closure expression. This approximation remains acceptable as long as the turbulent Mach number remains small, so that dilatational dissipation remains very small. It should be noted that in most applications of supersonic to hypersonic flows, the turbulent Mach number does remain small, i.e., far from unity [17].

In the current study, the extension of the LDKM model to compressible flows requires computing the local turbulent Prandtl number dynamically using the similarity hypothesis. At the test-scale level, the expression for the temperature and velocity correlation can be expressed exactly and the over-specified system is again solved using a least-square method, leading to a final expression:

$$1/Pr_t = -\frac{d_i n_i}{d_i d_i} \quad (3.39)$$

where

$$d_i = c_\nu \sqrt{k^{test}} \widehat{\Delta} \frac{1}{\langle \bar{\rho} \rangle} \left\langle \bar{\rho} \frac{\partial \widetilde{T}}{\partial x_i} \right\rangle \quad (3.40)$$

$$n_i = \frac{\langle \bar{\rho} \widetilde{u}_i \widetilde{T} \rangle}{\langle \bar{\rho} \rangle} - \frac{\langle \bar{\rho} \widetilde{u}_i \rangle \langle \bar{\rho} \widetilde{T} \rangle}{\langle \bar{\rho} \rangle} \quad (3.41)$$

Similarly, the closure coefficient for the pressure-dilatation correlation is evaluated from the test-scale pressure-dilatation correlation as:

$$\alpha_{pd} = \frac{C_\epsilon c^2}{\langle \widetilde{S} \rangle^2 \widehat{\Delta}^2 (P_{k^{test}} - D_{k^{test}})} \left(\left\langle \bar{P} \frac{\partial \widetilde{u}_i}{\partial x_i} \right\rangle - \langle \bar{P} \rangle \left\langle \frac{\partial \widetilde{u}_i}{\partial x_i} \right\rangle \right) \quad (3.42)$$

where c is the speed of sound.

The other coefficients σ_k and Sc_t could also be evaluated dynamically, if needed using a similar strategy. However, the impact of the σ_k is small compared to other terms in the governing equation for k^{sgs} , and is therefore, assumed to be constant ($\sigma_k = 1$). The turbulent Schmidt number is taken to be equal to 0.9. This latter approximation is acceptable for the simulation of cases where species play a passive role.

3.1.4 Realizability conditions

Vreman *et al* [56] showed that if a positive semi-definite filter, such as the top-hat filter, is used within an LES formulation, the subgrid stresses have to be positive semi-definite. These conditions, referred to as the *realizability* constraints, were found by Nelson and Menon [42] to be satisfied by the LDKM formulation for the computation of well-resolved and fully turbulent simulations. The strong and very localized variations induced by shocks can makes it difficult to satisfy this property over regions of the flow. Génin *et al* [24] showed that enforcing the weak realizability constraints was beneficial to the LES modeling of shock / isotropic turbulence interaction at low Mach numbers. The weak realizability constraint consists in enforcing:

$$\begin{cases} |\tau_{12}^{sgs}|^2 & \leq \tau_{11}^{sgs} \tau_{22}^{sgs} \\ |\tau_{23}^{sgs}|^2 & \leq \tau_{22}^{sgs} \tau_{33}^{sgs} \\ |\tau_{13}^{sgs}|^2 & \leq \tau_{11}^{sgs} \tau_{33}^{sgs} \end{cases} \quad (3.43)$$

With the closure adopted in the present study, these constraints are manipulated to show that the following relation should always hold:

$$c_\nu \leq \frac{\sqrt{k^{sgs}}}{\sqrt{3} \tilde{S} \Delta} \quad (3.44)$$

where

$$\tilde{S}^2 = \frac{1}{2} \left(\tilde{S}_{ij} - \frac{1}{3} \tilde{S}_{kk} \delta_{ij} \right) \left(\tilde{S}_{ij} - \frac{1}{3} \tilde{S}_{kk} \delta_{ij} \right) \quad (3.45)$$

The validity of the current closure approach to these constraints will be closely examined in the context of shock / turbulence interaction for strong shocks.

3.2 Hybrid Algorithm for Shock-Shear Simulation

An accurate simulation of turbulence in supersonic flows is made difficult by the very different scheme properties required within the same simulation. The resolution of turbulent structures requires a smooth-flow solver with limited numerical dissipation, whereas the discontinuities that can arise from supersonic flows require a significant amount of dissipation in order to be correctly captured. Shock-capturing methodologies have been developed to enable the simulations of supersonic and hypersonic flows, but even higher-order methods do not perform correctly in turbulent regions. Lee *et al* [35] found that the use of a 6th-order ENO scheme was too diffusive to properly capture turbulent features in a problem of shock / turbulence interaction.

Rather than trying to develop a single scheme that performs well in any region of a supersonic turbulent flow, a hybrid approach has been developed to enable such simulations. The base solver is a low-dissipation central scheme, adapted to the simulation of turbulent, reacting flows, which has extensively and successfully been used for practical studies of high Reynolds number reacting flows. This scheme is combined with a flux-difference splitting approach that permits the capture of flow discontinuities locally.

3.2.1 Description of the flux-difference splitting scheme

The upwind scheme used in the present formulation is a high-order flux difference splitting method. The reconstruction of the interface is performed using a MUSCL type interpolation [54] with a limiting function to ensure monotonicity. The monotized central limiter is adopted. The *reconstruction* of a variable U consists in extrapolating the variable to the interface with a directional bias, so that two states are obtained, left (U^L) and right (U^R), following the approach given by:

$$U_{i+1/2}^L = U_i + \frac{1 - \xi_i}{2} \phi_{mc}(r_{i-1/2}^+) \Delta_{i-1/2}(U)$$

$$U_{i+1/2}^R = U_{i+1} - \frac{1 - \xi_{i+1}}{2} \phi_{mc}(r_{i+3/2}^-) \Delta_{i+3/2}(U)$$

where $\Delta_{i+1/2}(U)$ is given by:

$$\Delta_{i+1/2}(U) = U_{i+1} - U_i$$

The limiting function, ϕ_{mc} used here is the monotized central limiter, which satisfies the symmetry condition as well as the TVD property [27]. It is given as:

$$\phi_{mc}(r) = \max\left[0, \min\left(2r, 2, \frac{1+r}{2}\right)\right]$$

where ξ_i is a coefficient determined by a flattening operation [12] used to prevent steep and strong gradients from creating unphysical oscillations in the post-shock region. This flattening is done by reducing the order of reconstruction on all variables when steep strong shocks are detected. A cell is identified as being part of a shock wave if the following two conditions are satisfied:

$$\frac{|P_{i+1} - P_{i-1}|}{\min(P_{i+1}, P_{i-1})} > \frac{1}{3} \quad (3.46)$$

$$u_{i+1} - u_{i-1} < 0 \quad (3.47)$$

The shock thickness is then measured by relating the pressure gradient across two zones to the gradient across four zones,

$$S_{p,i} = \frac{P_{i+1} - P_{i-1}}{P_{i+2} - P_{i-2}} \quad (3.48)$$

$$\tilde{\xi}_i = \max\left[0, \min\left(1, 10(S_{p,i} - 0.75)\right)\right] \quad (3.49)$$

The limiting factor ξ_i is then defined as:

$$\xi_i = \begin{cases} \max(\tilde{\xi}_i, \tilde{\xi}_{i+1}), & \text{if } P_{i+1} - P_{i-1} < 0 \\ \max(\tilde{\xi}_i, \tilde{\xi}_{i-1}), & \text{otherwise} \end{cases} \quad (3.50)$$

The reconstruction, equations 3.46 and 3.46 is then fully defined, and can be applied to various sets of variables ([4]). In the present work, the operation is performed on the primitive variables $(\bar{\rho}, \tilde{u}_i, \bar{P}, \rho_k)$. Additional variables if needed are then computed, and the monotonicity of these derived variables is explicitly checked and enforced. The monotonicity of the interface temperatures, for instance, are enforced by reducing the order of extrapolation of pressure and/or density as needed. The reconstruction of the species specific density is also performed with special attention. The most limiting factor of all specific densities is applied to all others, in order to ensure mass conservation at the cell interfaces.

Fluxes at the cells interfaces are then obtained through the resolution of the Riemann problem formed by the reconstructed state. The problem is solved using an approximate Riemann solver. In this work, a hybrid approximate Riemann solver has been developed, that permits a proper capture of the discontinuities in supersonic flows, while reducing the instabilities of other, classical, Riemann solvers. Its formulation is based on the combination of two solvers of the HLL- family ([27]).

The HLLC [53] approximate Riemann solver is based on an extension of the 2 – waves HLL-Riemann solvers for hydrodynamics problems, rather than on the formal 3 – waves *HLL*– solvers. Its formulation results in a computationally inexpensive, robust and yet accurate solver for the resolution of hydrodynamics problems, and compares well to other commonly used Riemann solvers (such as the Roe, Osher, Two-Shock, Two-Rarefaction Riemann solvers, see for *e.g.* [29], [21]) It is often preferred to the Roe-solver for its characteristics of positivity and entropy preservation. The known instability of this solver to odd-even decoupling and carbuncle phenomenon is cured by employing the HLLE Riemann solver ([18]), a truly 2 – waves HLL-solver for flux computation in the shock *transverse* directions (detected from equations 3.46 and 3.47). This hybrid solver has a reduced sensitivity to instabilities, and is found less dissipative than hybrid solvers, which use HLLE for all directions in the shock ([45]). In particular, the new solver recovers the accuracy of the HLLC Riemann solvers for the resolution of one-dimensional problems. Extension of the computational method to multi-dimensional problems is performed using an unsplit methodology. The hybrid Riemann solver does not show any instability to the odd-even decoupling, and accurately resolves the carbuncle test case [10]. More details on the HLLE and HLLC formulations are given in Appendix A

This method is integrated in the hybrid formulation by sensing strong discontinuity regions using a smoothness sensor. The switch used in this study is similar to that presented in [22] and applied to practical turbulent problems in [24]. The smooth-flow central scheme in LESLIE3D performs well for the resolution of turbulent flows, but cannot correctly simulate strong discontinuities. A smoothness parameter S_i is formulated based on variables curvatures ([39]):

$$S_i = \frac{|Q_{i+1} - 2Q_i + Q_{i-1}|}{|Q_{i+1} - Q_i| + |Q_i - Q_{i-1}|}, \quad (3.51)$$

where Q can be any variable of interest. Both pressure and density can be used to sense the smoothness of the flow. To prevent switching on numerical noise, a threshold value for the denominator is defined. The smoothness S_i is set to 0 if

either the numerator or the denominator is less than $0.06Q_i$. The cell is identified as *non-smooth* if the smoothness parameter exceeds a threshold value of 0.5. In multi-dimensional problems, the transverse fluxes to that cell are also tagged as non-smooth, and all fluxes are evaluated with the shock-capturing scheme. In all other cases, the smooth spatial discretization is used.

3.2.2 Validation of the flux-difference splitting scheme

The discontinuity-capturing method has been extensively tested and validated for a wide variety of flow configurations. Some representative tests are discussed here.

The shock-capturing capability is illustrated by *Noh's problem*. This test case simulates two *infinite* strength shocks moving outwards from the center of a one-dimensional domain. The initial conditions are given by a sharp separation at $x = 0.5$, where the left state is given by $(\rho, u, P) = (1, 1, 10^{-6})$, while the right state is $(\rho, u, P) = (1, -1, 10^{-6})$. The simulation is run for a total time $T = 1$. The problem is solved over a grid with 100 grid cells. Figure 3.1 shows the density profile at the end of the simulation using the current solver, and compared to a reference solution. In the course of the simulation, the shocks are captured at the right propagation speed. Furthermore, the post-shock profiles show very small oscillations, as a result of the flattening operation, leading to a proper resolution and proper shock propagation speed with limited dissipation. Only a slight dip is observed in the density profile, as a result of the transience in the formation of the shocks.

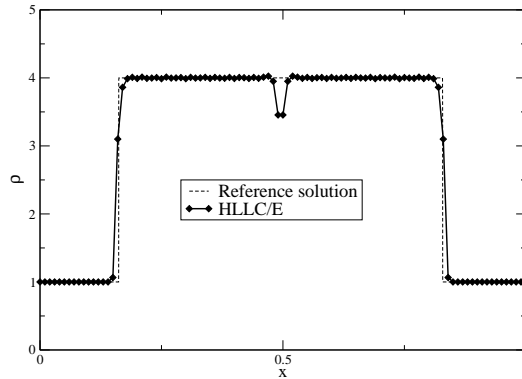


Figure 3.1: Density profile for two outwards-going infinite strength shocks.

The extension to multidimensional flow is demonstrated through the simulation of a point explosion problem of Sedov on a two-dimensional grid. 256×256 grid cells are used to discretize a $1m \times 1m$ domain with a uniform Cartesian grid. A cylindrical region of overpressure is initialized at the origin (bottom left corner) of the domain, over a radius of $3.33cm$. The pressure ratio across the initial discontinuity is $3.5 \cdot 10^6$. The strong blast wave generated by this energy deposition soon reaches a state of self-similar evolution. A high-resolution one-dimensional simulation of this problem in cylindrical coordinates is also performed for reference. Figure 3.2 represents the

one-dimensional projection of the (normalized) pressure of each grid cell versus the radius of the cell from the origin. The small scattering observed in this plot shows that the blast wave front is captured at its right speed, even when its propagation is not aligned with the cells. Furthermore, the capture of the shock front is relatively crisp, extending over two to three cells.

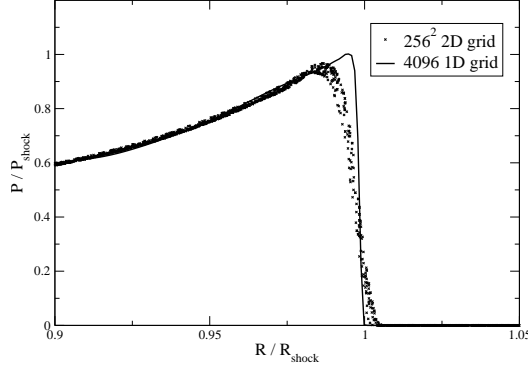


Figure 3.2: Sedov's point explosion pressure profiles.

The HLLC/E solver described earlier has been designed to reduce the sensitivity of the HLLC to a weakness shared by most classical Riemann solvers. The odd-even decoupling and carbuncle effect are solver's instabilities, that can lead to strong amplitude (unphysical) oscillations in the post-shock regions, which strongly perturb the flow, and can wrongly interact with turbulent structures. The Odd-Even decoupling test described by Liska and Wendroff [37] is repeated, using the HLLC/E solver. Strictly no instability is detected in that case, whereas similar simulations using the HLLC, the Two-Shock Riemann Solver and the Roe Riemann solver with Harten-Hyman entropy corrections showed very strong sensitiveness to the instability.

The classical test that highlights the carbuncle phenomenon has been conducted: the simulation of a $M = 10$ flow over a circular blunt body is performed. A grid with 80×160 cells is used to resolve this problem. Figure 3.3 shows the temperature iso-lines from the computations using the HLLE, the HLLC, the Roe, the Two-Shock Riemann Solver (TSRS) [52], and the HLLC/E solvers. The result obtained with the HLLE solver can be used as reference, while the other computations show an instability along the main shock front, leading to the formation of spurious oscillations in the post-shock region. The solver of Roe is particularly sensitive to this instability, whereas the HLLC/E does show a small kink within the shock front, but its instability appears as very small when compared to the other solvers. This study validates the HLLC/E hybrid solver and its reduced instability.

3.2.3 Validation of the LES methodology

The algorithms developed in the current effort and described earlier have been used to study high-speed compressible turbulence using both DNS and LES, as well as some

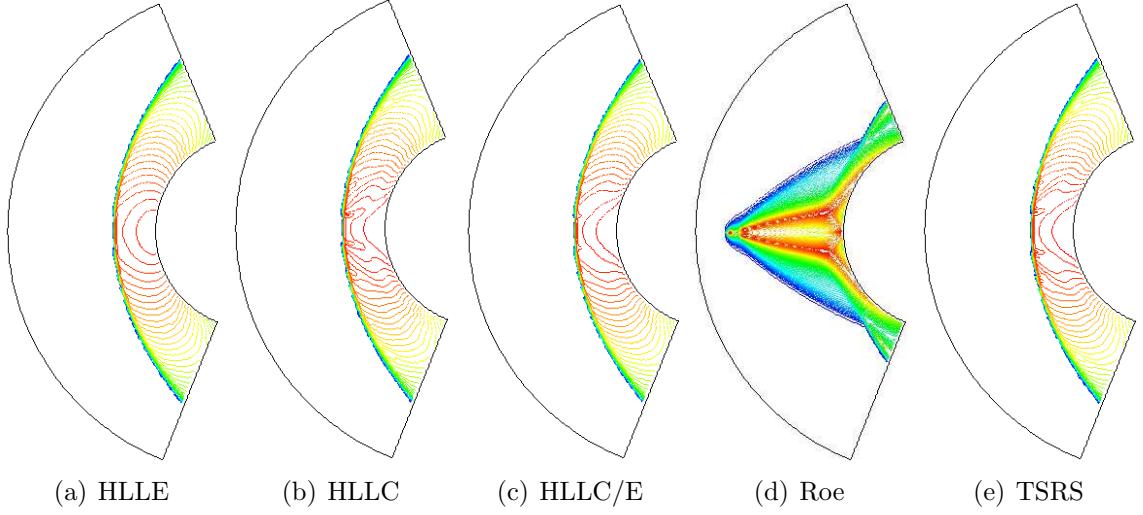


Figure 3.3: Carbuncle test case using contact-preserving and mixed Riemann Solvers

canonical test problems. The hybrid scheme designed to capture strong discontinuities and to resolve the smooth variations is used to study the *Shu – Osher* [51] test problem. This test-case consists in a one-dimensional shock front propagating into a sinusoidal density distribution. The interaction forms a region of rapid oscillations in the post-shock region which steepen into shocks, forming an N-wave pattern. A correct resolution of this problem requires an accurate computation of shock propagation at the right speed, and a proper capture of the short-wavelength smooth variations that form in the post-shock region.

The initial conditions for this problem are given by the following density profile:

$$\rho(x) = \begin{cases} 3.857142 & x < 2 \\ 1 - 0.2 \sin(5x) & x \geq 2 \end{cases} . \quad (3.52)$$

The traveling shock is initialized at $x = 2$, and the pre-shock pressure and velocity are set 1 and 0, respectively. The post-shock values for pressure and velocity are constant and equal to 10.333333 and 2.629369, respectively. A calorically perfect gas is simulated with an adiabatic index γ of 1.4. The simulation is run for a total time of 1.872.

The purely upwind approach cannot capture short wavelength oscillations when 200 grid cells are employed (Fig. 3.4), and in this region the dominant wavenumber of the N-wave pattern appears as the smallest resolved wavenumber. Employing the hybrid method permits for the same resolution to crisply capture the shock with the upwind scheme, while the smooth flow solver is used to resolve the post-shock medium. As a result, despite the fact that the full amplitude of the oscillations is not totally recovered, the short wavelengths are apparent in the post-shock region. Increasing the resolution to 400 grid cells confirms the low-resolution observation. The upwind approach captures all the wavelengths of the problem, but the inherent dissipation of the scheme prevents this approach from capturing the oscillations amplitude. The

hybrid approach combines the advantages of both schemes, leading to a proper capture of the main shock and a very good resolution of the post-shock oscillations.

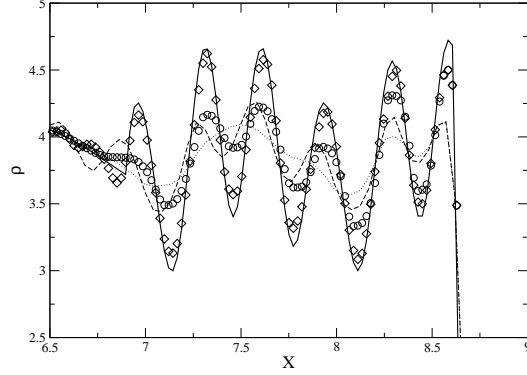


Figure 3.4: Evolution of the density for the Shu-Osher problem. —, Hybrid (N=200) - - -, pure upwind (N=200) ···, Hybrid (N=400) ◇, pure upwind (N=400) ○

The study of multi-mode Richtmyer-Meshkov Instabilities is shown next. A domain of $0.04cm \times 0.01cm$ is discretized using 1024×256 grid cells. An initial interface between hydrogen at an initial temperature of $300K$ and helium at $4500K$ is shaped by superposing a primary perturbation (of wavelength $0.01cm$ and amplitude $0.001cm$) and a secondary perturbation (with a wavelength of $0.002cm$ and $1/7th$ of the primary amplitude). A shock with an overpressure ratio of 300 propagates in the region containing helium, towards the shaped interface. The interaction leads to a 180° phase inversion. The initially smooth interface forms large and small scale vortices under the effect of baroclinic torque, which transition to turbulence and eventually decay. The shock is partially transmitted in the hydrogen region, and is regularly distorted by a series of transverse waves that form local triple points. The slip lines so formed form a *diamond – shaped* pattern, which creates vortical structures due to Kelvin-Helmholtz instabilities. This problem has been solved using the hybrid methodology with both the Piecewise Parabolic Method (PPM) and with the current HLLC/E upwind scheme. The PPM implementation is identical to that of the PROMETHEUS code and the FLASH code developed in the university of Chicago [23], and its integration in the hybrid methodology has been performed and described earlier [22]. Fig. 3.5 shows the temperature fields for all computations, and the regions where upwinding is used in the fluxes computation. The large structures formed through the interaction are found identical with both methods. The small scale vortices are found to be slightly different for the two cases, but comparable. The regions of upwinding are significantly more important in the case when PPM is used for discontinuity capturing purposes, as illustrated in Fig. 3.5. The directional splitting used in the PPM method requires an updated of all the neighboring cells, hence broadening the stencil of PPM usage in the hybrid formulation. The unsplit HLLC/E method, on the other hand, used the same integration method as the smooth flows solver, and can then be locally activated. It leads then to a smaller region of activation around the density

interfaces, hence, a reduced use of the dissipative scheme.

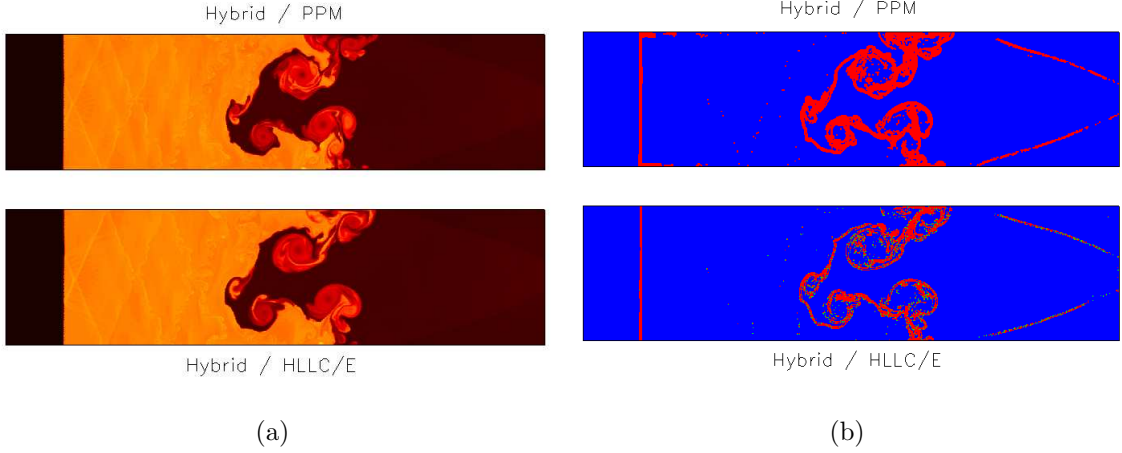


Figure 3.5: Simulations of multi-mode Richtmyer-Meshkov instabilities using hybrid PPM/4th (top) and hybrid HLLCE/4th (bottom): Temperature fields (left) and switch fields (right).

The Richtmyer-Meshkov Instability (RMI) problem, used here to highlight the switching process and for comparison of the hybrid methods, is a fundamental instability in shock containing flows. The mixing induced through the interaction and the turbulence generated by the long-time decay, and/or by a re-shock make this case a computational challenge. This configuration will be re-examined later using LES as well.

The hybrid scheme can reliably capture shocks and still apply a limited amount of dissipation on the turbulent structures. The closure model is evaluated by doing LES and comparing with DNS using the current code and also with reference DNS results [40], [35]. The DNS studies have been used in *a priori* studies to highlight the driving terms of the k^{sgs} governing equation within this configuration. The LES grid used to discretize the configuration shown in Fig. 3.6 is coarser by a factor of 13 compared to the DNS grids. The resolution in the direction across the shock region is the same spacing as in the DNS in order to capture the shock but the resolution in the other two directions were reduced drastically. The initializations of the LES simulation is obtained from the filtered DNS field.

The time-averaged axial Reynolds stress profiles obtained from the calculations of the $M = 1.29$ and $M = 3.0$ cases are shown in Fig. 3.7 along with their corresponding filtered DNS fields. In these plots, k_0 denotes the most energetic wavenumber in the initial turbulent field used at the inflow, and is used to normalize the distance from the inflow. The results of the LES using the LDKM approach are shown along with the results of an under-resolved simulation without the closure model. The turbulent decay that occurs before the interaction is well captured at the right rate, when the explicit subgrid model is used. Without model, the turbulent decay is off for the low

Mach number case. No real trend can be isolated from the highest Mach number case, as the timescale for convection of the turbulent structures is significantly smaller than the timescales for production and/or dissipation. The post-shock level of stresses is correctly predicted by the numerical method. The peak values reached downstream the shock, from the acoustic / kinetic energy transfer, are slightly under-estimated in both cases. Even though the minimum spacing matches that of the DNS simulation, the grid around the shock is coarser, and leads to a slight under-prediction. The dynamic model is, however seen to reproduce the gain in turbulence in the post-shock region correctly. The turbulent decay that follows is captured at the right rate when the LDKM is used. The absence of model, on the other hand, fails to capture the turbulent behavior. The molecular viscosity in this under-resolved does not provide enough dissipation to reproduce the filtered DNS profiles.

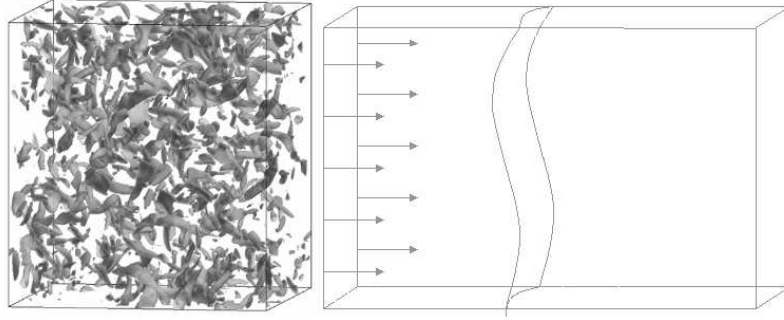


Figure 3.6: Computational set-up for the simulation of shock / isotropic turbulence interaction. A box of isotropic turbulence is used at the inflow of a spatial, shock-fixed domain.

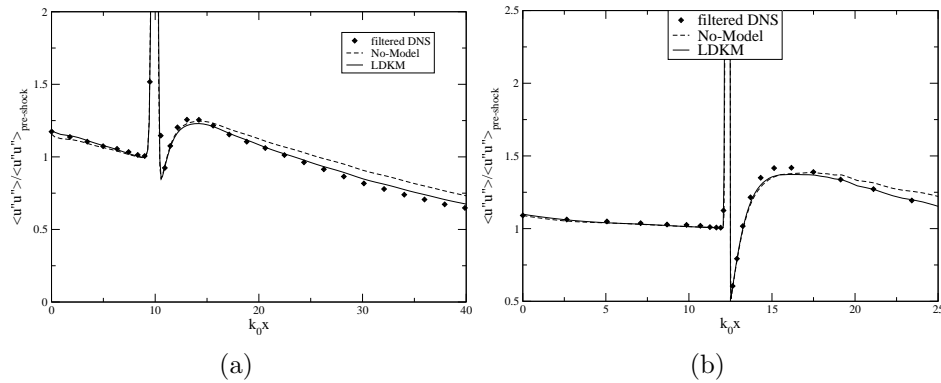


Figure 3.7: Longitudinal Re-stress profiles for a $M = 1.29$ Shock (left) and a $M = 3.0$ shock (right) interacting with an isotropic turbulent field.

The results presented in this section highlight the different aspects of the algorithms developed in this research. The upwind scheme permits a proper capture of the shock waves over $2/3$ cells, and with the proper propagation speed. The hybrid scheme combines this upwind method to a smooth central scheme adapted to turbulent flows simulation. This hybrid scheme successfully captures the problem of Shu-Osher, shock / turbulence interaction. Furthermore, the development of the LDKM closure approach have permitted a good capture of the turbulent behaviors for this interaction without requiring any ad hoc model adjustment. In fact, the entire algorithm (both numerical and subgrid) developed in this effort requires no model adjustments in any of the reported flows (see next section). The application of this method to different flows of practical interest is presented next.

CHAPTER IV

RESULTS AND DISCUSSION

4.1 Richtmyer-Meshkov Instability

A Richtmyer-Meshkov Instability (RMI) is the result of an impulsive acceleration of an interface between two media of different densities. The initial density discontinuity leads to the formation of a momentum interface and of a mixing region which grows linearly in the early time of the experiment. When non-linearities start playing a major role, the large-scale structures start breaking down, and a region of turbulence is formed from the initial interface.

Classically, the impulse needed in experimental studies of Richtmyer-Meshkov instabilities is provided by a traveling shock. As the shocks travel down the shock tubes, they reflect from the back wall of the experimental facility, and *re-shock* the mixing region. This was observed to accelerate the transition to turbulence for this instability. One of the experiments presented by Vetter and Sturtevant [55] has been studied numerically with the current LES methodology. A $M = 1.98$ shock interacts with an *Air/SF₆* interface, leading to an initial RMI, which forms large coherent structures. The shock reflection from the back-wall re-shocks the mixing zone, and transition to turbulence is enhanced. Experimental measurements of the mixing zone are used for comparison. The domain employed for the current simulation is a 0.59m long with a $0.27m^2$ cross section shock tube, and is schematically shown in Fig. 4.1. Periodic conditions are enforced in y and z direction. The right boundary was set as a no-flux wall, whereas the left boundary is treated as an outflow.

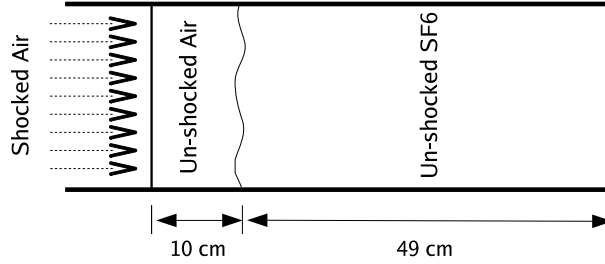


Figure 4.1: Geometry of the Simulation

In the numerical simulation, the interface between air and SF_6 is initialized as: $x_I(y, z) = a_0 |\sin(\pi y/\lambda) \sin(\pi z/\lambda)| + a_1 h(y, z)$, where $h(y, z)$ is a random function, which perturbs the initial interface profile to break the symmetry and enhance perturbation and transition. Here, $a_0 = 0.25cm$, $a_1 = 0.025cm$ and $\lambda = 0.27/14cm$ are

Case	1	2	3	4
Physical Size (m)	0.59×0.27^2	0.59×0.27^2	0.59×0.27^2	0.59×0.135^2
Grid Size	281×129^2	420×193^2	560×257^2	560×129^2
Grid Resolution (cm)	0.21	0.14	0.105	0.105
Simulation Time (ms)	8.0	6.0	6.0	6.0
CPU hours	780	1680	7360	2040

Table 4.1: Grid resolution and domain size for various test cases

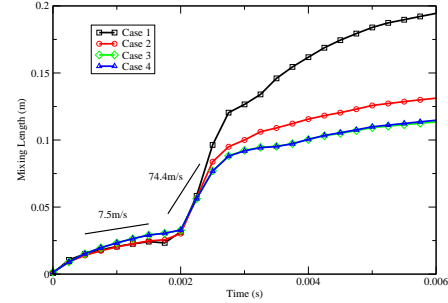
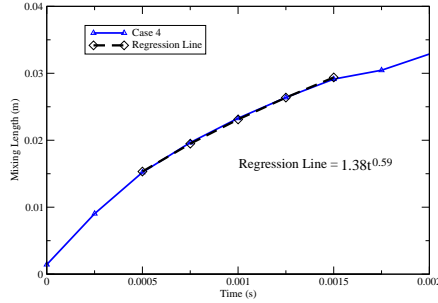
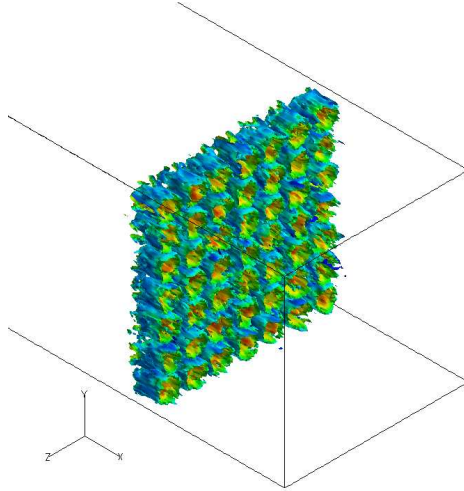


Figure 4.2: Mixing length before reshock **Figure 4.3:** Overall mixing length growth

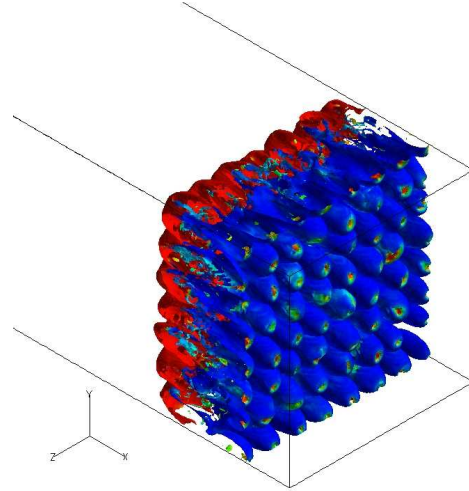
assumed [28]. Resolution and domain size studies have been performed. Four test cases (Table 4.1) are discussed here.

Vetter and Sturtevant [55] estimated the instantaneous mixing lengths from visual estimates of Schlieren images. The numerical mixing length is defined as $h(t) = 4 \int_{tube} (1 - \langle \psi \rangle) \langle \psi \rangle dx$, where $\langle \rangle$ represents the planar average. The growth rate before reshock can be often represented as $h_i(t) = a\tau^\theta$, where h represents the mixing length, a is a constant, and τ is linear function of the time [59]. Zhou [60] found that θ_b varies between 0.2 and $2/3$. The present simulation falls in the range of predicted values, with $\theta = 0.59$ (Fig. 4.2). Figure 4.3 clearly shows that the mixing width is over-predicted by the coarse grid but Cases 3 & 4 show that the mixing length do not depend on the largest scale of physical domain, and that a reduced physical length can be used. There is good agreement with the experimental data [55].

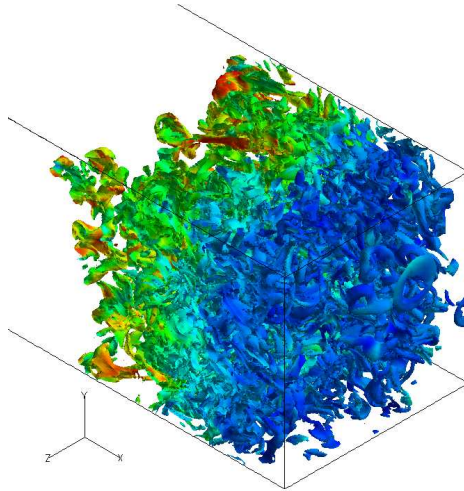
A time sequence of iso-vorticity contours is shown in Fig. 4.4. Figs. 4.4(a) and 4.4(b) show the structural evolution from the first shock / interface interaction. The formation of large *finger*-like shapes is initiated from the instability. These structures grow in the linear regime, and very high levels of vorticity are obtained. These structures would eventually transition to turbulence and decay. The re-shock, however, enhances this instability, and Figs. 4.4(c) and 4.4(d) show the vortical structures after the second passage of the shock. It is observed that the large, organized structures have broken down as a result of the interaction, forming a wide mixing region with numerous vortical structures of different scales. 2D spectra of the axial velocity



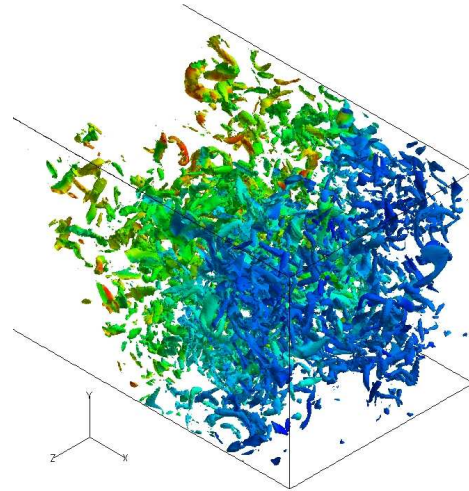
(a) 1.5ms, 4000(1/s)



(b) 2.25ms, 8000(1/s)



(c) 4.0ms, 8000(1/s)



(d) 5.0ms, 8000(1/s)

Figure 4.4: Iso-surface of total vorticity magnitude, colored by mass ratio of air

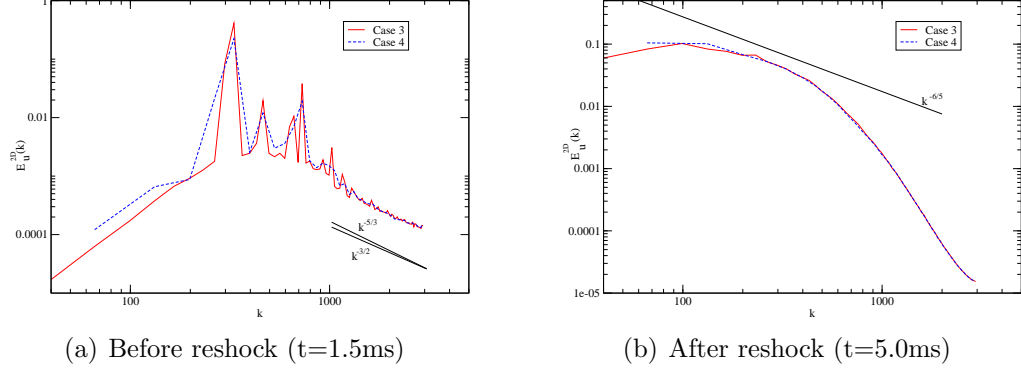


Figure 4.5: 2D Spectra of the x-component of velocity

within the mixing zone (defined as the region where $\psi \geq 0.1$) are presented in Fig. 4.5. The dominant wavenumber imposed at the initialization and its harmonics are persistent in the spectra shown in Figs. 4.5(a). This is in accordance with the large-scale structures observed from the iso-vorticity contours. Again, the late development would dissipate the dominant waves and allow the formation of turbulent structures. However, re-shocking is achieved before this transition stage is reached. Figure 4.5(b) shows the spectrum obtained after re-shock. The second interaction enhances the mixing, and a wider spectrum is obtained without dominant frequency. Zhou [59] analytically derived that the energy spectrum of the RMI shows a $k^{-3/2}$ scaling, rather than the classical $k^{-5/3}$, due to inhomogeneity and anisotropy induced by the shock motion. In the spectra, an inertial range is obtained, although the dominant slope does not match exactly the theoretical values $k^{-3/2}$ or $k^{-5/3}$, but is closer to $k^{-6/5}$. This latter scaling was also obtained in another LES study [11] but is currently still being investigated.

The RMI is a challenging problem in numerical studies, as it evolves from a sharp density interface. As such, the scheme is required to capture strong discontinuities with limited dispersion, and still show small dissipation in order to capture the most unstable modes of the configuration. The late-stage developments of instability lead to the formation of high strain and high vorticity regions, which eventually form turbulence. As noted before, re-shocking the interface only accelerates this process. This second stage requires a high resolution scheme with low dissipation, and a correct subgrid modeling that will mimic turbulence generation and the subsequent turbulent decay.

4.2 Regular and Irregular Cellular Detonations

In a detonation wave, a high-speed shock travels in a low-temperature reactive mixture, compressing and heating the gases. In the post-shock region, the conditions to achieve auto-ignition are reached. The heat released by the reaction and the gas expansion *feed* back into the main wave. A good capture of the phenomenon requires a

proper resolution of the running shock, an accurate treatment of the chemical source terms, and a low dissipation resolution in the post-shock region in order to capture the turbulent structures emanating from the triple points on the detonation front.

Simulation of regular and irregular cellular detonations is challenging as it involves large range of length and time scales, nonlinear coupling between chemistry and fluid dynamics and instability in flow. Different detonations have been simulated, and two cases are presented hereafter, one of regular and one of irregular nature (see Table 4.2). The initial profiles of pressure, temperature and species mass fractions are obtained using a one-dimensional steady-state (ZND) detonation solver. These profiles are projected on a two-dimensional grid, and the perturbation that transitions to the cellular structure formation is initiated by placing a pocket of unreacted mixture behind the front ([43]).

Case	Type	Resolution	Cell resolution ($\Delta x = \Delta y$) μm .	CPU hours used
I	Regular	4800X1200	7.25	1665
II	Irregular	4000X2000	18.75	2850

Table 4.2: Resolution for regular and irregular detonation simulations.

First, a detonation with regular cellular structures is presented: Case I considers the regular detonation obtained for a stoichiometric mixture where γ is 1.2, the initial temperature (T_0) 293K, the initial pressure 0.2atm., the activation energy (Ea/RT_0) is 50 and the heat released by the reaction is given by $Q/RT_0 = 50$. Here, R is universal gas constant. The Chapman-Jouguet (CJ) detonation speed (D_{CJ}) is the most likely detonation speed, and is, for this case, 1.8km/s. The overdrive parameter ($f = (D/D_{CJ})^2$) is 1.6, where D is actual detonation speed. Recording the spatial evolution of the triple points tracks leads to a *numerical soot foil track*. Figure 4.6 shows the regular cells formed for Case I. This track is compared to the numerical results of Deiterding [14] for the same conditions.

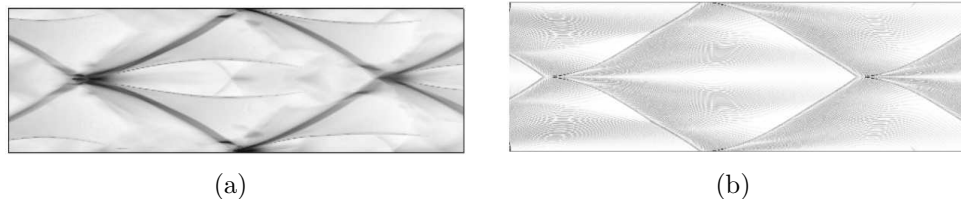


Figure 4.6: Numerical soot foil recording maximum pressure showing regular cellular structures from the current simulation (left) and from Deiterding [14] (right).

Case II is for an irregular detonation. The physical parameters for this case are: $\gamma = 1.228$, $Ea/RT_0 = 38.2$ and $Q/RT_0 = 34$, and the overdrive factor is $f =$

1.4. Figure 4.7 shows the sootfoil for this configuration along with an instantaneous capture of the detonation front, represented through a snapshot of the field of density gradient. The sootfoil shows the irregularity of the cells formed by the triple points. Some triple points fade out as a consequence of the weak transverse waves induced in this case. The instantaneous field also shows some of the vortical structures induced by the triple point from baroclinic effects and Kelvin-Helmholtz instabilities. The complex nature of the irregular detonation comes from the interaction between the transverse waves, the vorticity and the heat released from the reaction.

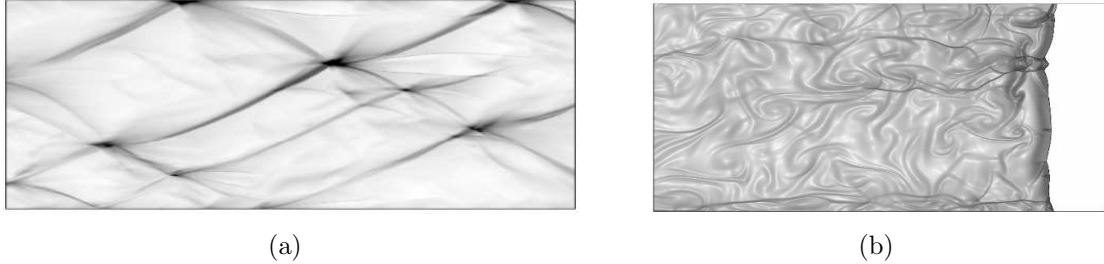


Figure 4.7: Numerical soot foil (left) and instantaneous field of density gradient (right) for an irregular detonation (case II)

Full 3D LES of detonation has also been studied. A case of detonation is simulated in a mixture of $2H_2/1O_2/3Ar$ initially at a pressure of $26kPa$ and a temperature of $300K$, similar to the experiments of [6]. A 7-steps H_2/O_2 reaction mechanism is employed to treat the combustion [20], and $500 \times 180 \times 180$ grid cells are used to discretize a physical domain of dimensions $8cm \times 1.25cm \times 1.25cm$. Figure 4.8 shows a snapshot of the detonation structure. The transverse waves in two dimensions are clearly identified from the pressure gradient field. Their regular structure in three dimensions is illustrated by the regular pattern of instabilities that corrugate the main front of iso-pressure. Also, the unsteady triple points create vortical structures in the post-detonation region that lead, through Kelvin-Helmholtz instabilities, to turbulent structures further downstream. The cell width obtained from this simulations is predicted in close agreement to the experimental observations.

The evolution of the detonation front in three-dimensional simulations requires the use of an upwind, shock-capturing scheme. Clearly, the downstream evolution which depends on the regularity of the detonation is showing unstable vortical structures, and as the detonation becomes more unstable, the level of post-detonation turbulence can significantly increase. The hybris method appears well adapted to capture of such complex detonative processes.

4.3 Shock-Shear Interactions in a Scramjet

Facing the problem of reduced mixing in high-speed shear layers, and motivated by the experimental and analytical prediction of turbulence enhancement through shocks,

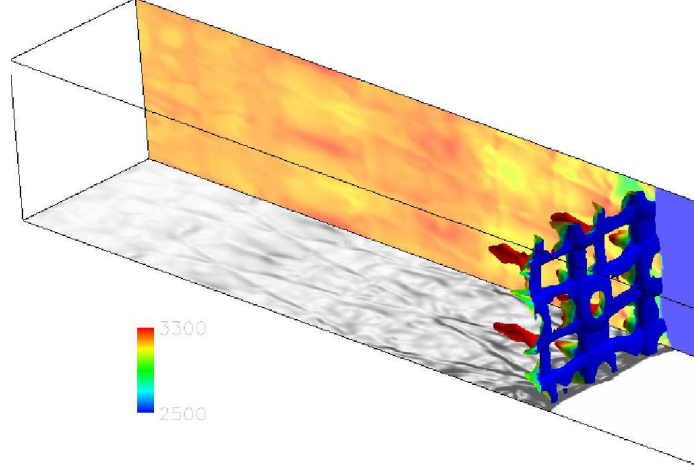


Figure 4.8: Three-dimensional LES results of the pressure iso-surface of $700kPa$, colored by the temperature field. The temperature field is shown in the last plane, and the pressure gradient magnitude is on the bottom plane.

many researchers have studied the development of *shocked* turbulent shear layers. The physical processes occurring during a shock / turbulent shear layer interaction are, however, numerous and not limited to shock / turbulence. The vorticity of the large coherent structures is amplified through the strong compression. Also, density gradients across the shear layer can lead the formation of local Richtmyer-Meshkov instabilities if misaligned with the shock's pressure gradients. Finally, the mean vorticity within a shear layer does not necessarily increase through the interaction.

The configuration studied numerically is that of a two-streams binary mixing layer ([15]). The upper stream (hereafter, denoted with a subscript u) is a mixture of N_2/H_2 , with 10% hydrogen in mass, with a static temperature of $2000K$ and a static pressure of $1atm$, flowing at Mach 2.0 (which corresponds to a velocity of $2672m/s$ with the thermally perfect gas Equation Of State (EOS) employed here). The lower stream (hereafter, denoted with a subscript l) is that of air where the static temperature and pressure are set to match that of the upper stream. The Mach number is set to 2.0, which corresponds to a velocity of $1729m/s$. Again, a thermally perfect gas EOS is used for this stream species. A schematic of the configuration studied here is shown in Fig. 4.9 The convective velocity for this flow is about $U_c = 2100m/s$. The convective Mach number is $M_c = 0.43$, which makes it moderately compressible, with turbulent structures that still resemble those of the incompressible mixing layer. In order to trigger the transition of this initially laminar profile, a random phase velocity perturbation is added to the mean profile with a fixed energy spectrum.

The problem was discretized using $250 \times 80 \times 40$ grid cells to resolve a domain of extent $0.17m \times 0.10m \times 0.03m$. Fig. 4.10 shows a top view of the iso-surfaces of the Q -criterion for the base mixing layer and the shocked counter-part. This

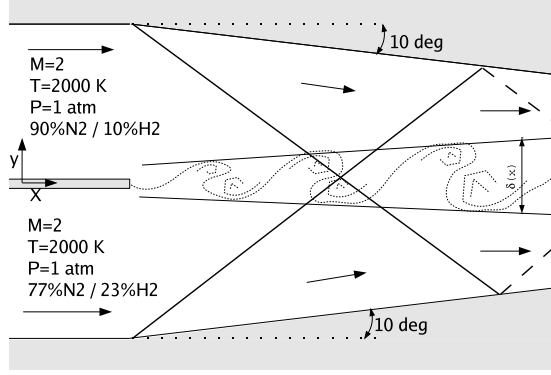


Figure 4.9: Sketch of the shocked mixing layer configuration.

variable, defined as the second invariant of the velocity gradient tensor, is well-suited for vortical field identification ([16]). These snapshots are taken at the same physical

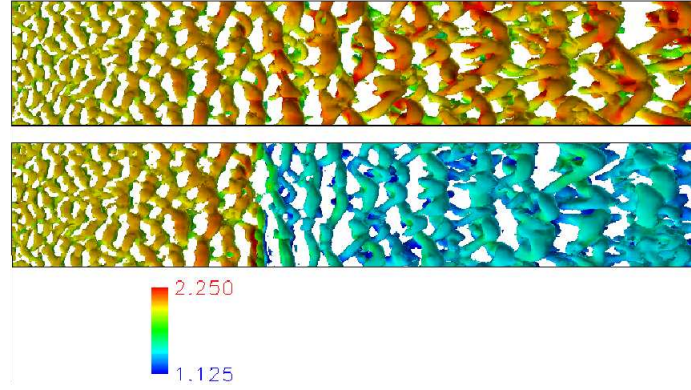


Figure 4.10: Iso-surface of the Q -criterion ($Q = 10^9 s^{-2}$) for the un-shocked (top) and the shocked (bottom) mixing layer, colored by the local Mach number (flow is from left to right)

time, after 10 flow-through-times. A fast transition to turbulence is initiated by the forcing at the inflow of the simulation, leading to a fully developed turbulent mixing layer. Strongly three-dimensional coherent structures are observed in the mixing layer. These coherent structures, initiated by natural instabilities of the flow, trigger and maintain the turbulence within the mixing layer thickness.

The shock impact is found to amplify all the turbulent levels within the mixing zone. In particular, the turbulent fluctuations in the cross-wise direction and the principal Reynolds stress R_{xy} are significantly enhanced through the interaction. As a consequence, the vortical structures in the shocked mixing layer are compressed, and show more two-dimensionality than in the un-shocked case, as is visible in Fig. 4.10. Later downstream, these structures recover a strong three-dimensionality. Furthermore, these increases in turbulent levels lead to an important increase in the mixing

efficiency in the region that follows the shocks. The thickness based on the 90%- H_2 mass fraction is shown in Fig. 4.11(a) for the base mixing layer and for the shocked shear layer. A reduction of the thickness is observed first as the shock interacts with the mixing region. This is due to the spatial compression of the mixing region by the two shocks, and should not be interpreted as a reduction in mixing efficiency. On the contrary, the shocked layer evolves with an increased growth rate in the region that follows the interaction. The growth rate is found to be double the growth rate of the un-perturbed layer. This observation is confirmed by the profile of mass entrained by the mixing layer, showed in 4.11(b). The mixing achieved through the shock impact is significantly greater than in the case of the base mixing layer.

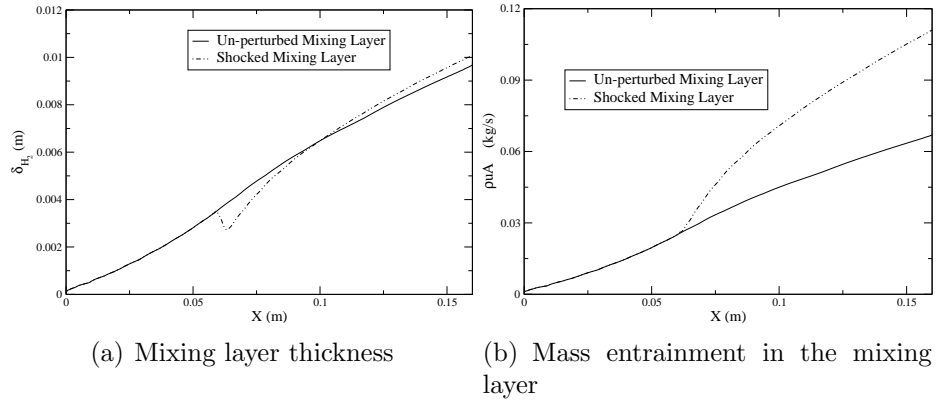


Figure 4.11: Mixing Layers growth rate based on a 90% H_2 mass fraction, and mass entrainment within the mixing layer thickness

Within 6cm from the location of the interaction, the mixing layer growth rate steadies out at a value that is about 6% higher than its unshocked counter-part, and the turbulent fluctuations relax to their un-disturbed levels. The reduction in the mean levels of vorticity in this configuration leads to a lower amount of turbulent production across the layer.

The effects of the shocks on the turbulent evolution and on the mixing efficiency are found to be strong, but quite localized in space. These results are in agreement with some experimental observations [50] where an increase in the growth rate was observed following the interaction with the shocks, with a relaxation to the un-disturbed levels observed within some short distance from the point of impact. It should also be noted, as pointed out by Drummond *et al* [15], that the shocks interaction also impact the static temperature within the layer, hence enhancing the reactions rates in the mixing zone. Considering that shock waves cannot be avoided in practical Scramjet engines, this method can be considered an interesting mixing-augmenting technique.

CHAPTER V

CONCLUSIONS AND FUTURE PLANS

A LES methodology has been presented that permits the resolution of compressible turbulent flows in supersonic environments. Two key developments were required to achieve this goal: a new hybrid numerical algorithm that captures strong shocks and shear turbulence, and a localized dynamic subgrid closure for compressible flows. The hybrid numerical algorithm combined a shock capturing approach with a shock-free algorithm using an automatic shock detection technique and has been validated for various canonical flows containing strong shocks as well as in flows with shock-turbulence interactions. It is shown that this algorithm has the requisite accuracy to do DNS of such flows. Subsequently, an advanced closure model for the subgrid kinetic energy equation has been developed and validated. The LDKM approach allows localized evaluation of all model coefficients during the simulation and therefore, there are no adjustable parameters in the proposed simulation strategy.

This new LES approach has been used for the study of various applications. A case of re-shocked Richtmyer-Meshkov Instability is discussed that highlights the importance of capturing the pressure and the density discontinuities until a high level of vorticity is achieved and transition to turbulence occurs. Also, fundamental studies of regular and irregular detonations are conducted showing how the post-detonation region is subject to the formation of vortical structures, which in 3D lead to the formation of a turbulent medium. Finally, the evolution of a turbulent shear layer after its interaction with two symmetric shocks is studied. An increased level of turbulence was captured behind the interaction point, leading to an enhanced growth rate. This phenomenon, associated to the increase in static temperature make this mixing augmentation technique apparently well suited for flame initiation and stabilization in supersonic flows. The amplified turbulence is, however, found to decay within a short distance from the interaction.

The LES approach developed here appears well adapted to the simulations of high-speed turbulent flows. Its applicability to practical configurations has been demonstrated. The resolution requirements can, however, increase significantly as the domains become more and more complex. A next step in the developments of this LES strategy will consist in implementing an Adaptive Mesh Refinement (AMR) technique. This method, which permits the grid to automatically adjust its levels of refinement is ideally suited within the hybrid framework developed in this effort.

Bibliography

- [1] B. Aupoix, G. A. Blaisdell, W. C. Reynolds, and O. Zeman. Modeling the turbulent kinetic energy equation for compressible turbulence. *Center for Turbulence Research, Proceedings of the Summer Program*, 1990.
- [2] K. R. Bates, N. Nikiforakis, and D. Holder. Richtmyer-meshkov instability induced by the interaction of a shock wave with a rectangular block of sf_6 . *Physics of Fluids*, 19, 2007.
- [3] P. Batten, N. Clarke, C. Lambert, and D. M. Causon. On the choice of wavespeeds for the HLLC riemann solver. *SIAM Journal of Scientific Computing*, 18(6):1553–1570, 1997.
- [4] C. Berthon. Stability of the muscl schemes for the euler equations. *Communications in Mathematical Sciences*, 3(2):133–157, 2005.
- [5] M. Brouillette. The richtmyer-meshkov instability. *Annu. Rev, Fluid Mech*, 34:445–468, 2002.
- [6] R. O. Carvel, G. O. Thomas, and C. J. Brown. Some observations of detonation propagation through a gas containing dust particles in suspension. *Shock Waves*, 13:83–89, 2003.
- [7] V.K. Chakravarthy and S. Menon. Large-eddy simulations of turbulent premixed flames in the flamelet regime. *Combustion Science and Technology*, 162:175–222, 2001.
- [8] V.K. Chakravarthy and S. Menon. Linear-eddy simulations of reynolds and schmidt number dependencies in turbulent scalar mixing. *Physics of Fluids*, 13:488–499, 2001.
- [9] P. R. Chapman and J. M. Jacobs. Experiments on the three-dimensional incompressible richtmyer-meshkov instability. *Physics of Fluids*, 18(074101), 2006.
- [10] Y. Chauvat, J.-M. Moschetta, and J. Gressier. Shock wave numerical structure and the carbuncle phenomenon. *International Journal for Numerical Methods in Fluids*, 47:903–909, 2005.
- [11] R. C. Cohen, W. P. Dannevik, A. M. Dimits, D. E. Eliason, A. A. Mirin, Y. Zhou, D. H. Porter, and P. R. Woodward. Three-dimensional simulation of a richtmyer-meshkov instability with a two-scale initial perturbation. *Physics of Fluids*, 14(10):3692–3709, 2002.
- [12] P. Colella and P. Woodward. The piecewise-parabolic method for hydrodynamics. *Journal of Computational Physics*, 54:174, 1984.

- [13] S. F. Davis. Simplified second-order godunov-type methods. *SIAM J. Sci. Stat. Comput.*, 9:445–473, 1988.
- [14] R. Deiterding. *Parallel Adaptive Simulation of Multi-dimensional Detonation Structures*. PhD thesis, Brandenburgischen Technischen Universität Cottbus, 2003.
- [15] J. P. Drummond and H. S. Mukunda. A numerical study of mixing enhancement in supersonic reacting flow fields. *AIAA-88-3260*, 1989.
- [16] Y. Dubief and F. Delcayre. On coherent-vortex identification in turbulence. *Journal of Turbulence*, 1, 2000.
- [17] J.-P. Dussauge. Compressible turbulence of supersonic flows: actions and interactions. *Conference on Turbulence and Interactions TI2006, May 29 June 2, 2006, Porquerolles, France*, 2006.
- [18] B. Einfeldt. On godunov-type methods for gas dynamics. *SIAM J. Numer. Anal.*, 25(2):294–318, 1988.
- [19] B. Einfeldt, C. D. Munz, P. L. Roe, and B. Sjogreen. On godunov-type methods near low densities. *Journal of Computational Physics*, 92:273–295, 1991.
- [20] D. R. Eklund, J. P. Drummond, and H. A. Hassan. Calculation of supersonic turbulent reacting coaxial jets. *AIAA Journal*, 28(9):1633–1641, 1990.
- [21] K. S. Erduran, V. Kutija, and C. J. M. Hewett. Performance of finite volume solutions to the shallow water equations with shock-capturing schemes. *International Journal for Numerical Methods in Fluids*, 40:1237–1273, 2002.
- [22] B. Fryxell and S. Menon. Large-eddy simulation of richtmeyer-meshkov instability. *AIAA Paper 2005-0314*, 2005.
- [23] B. Fryxell, K. Olson, P. Ricker, F. X. Timmes, M. Zingale, D. Q. Lamb, P. MacNeice, R. Rosner, J. W. Truran, and H. Tufo. Flash: An adaptive mesh hydrodynamics code for modeling astrophysical thermonuclear flashes. *The Astrophysical Journal Supplement Series*, 131:273–334, 2000.
- [24] F. Génin, B. Fryxell, and S. Menon. Hybrid large-eddy simulation of detonations in reactive mixtures. *20th International Colloquium on the Dynamics of Explosions and Reactive Systems*, 2005.
- [25] F. Génin, B. Fryxell, and S. Menon. Simulation of detonation propagation in turbulent gas-solid reactive mixtures. *AIAA Paper 2005-3967*, 2005.
- [26] S. Gordon and B. J. McBride. Computer program for calculation of complex chemical equilibrium compositions and applications. NASA Reference Publication 1311, NASA, 1994.

- [27] A. Harten, P. D. Lax, and B. van Leer. On upstream differencing and godunov-type schemes for hyperbolic conservation laws. *SIAM Review*, 25:35–61, 1983.
- [28] D. J. Hill, C. Pantano, and D. I. Pullin. Large-eddy simulation and multiscale modelling of a richtmyermeshkov instability with reshock. *Journal of Fluid Mechanics*, 557:29–61, 2006.
- [29] M. J. Ivings, D. M. Causon, and E. F. Toro. On riemann solvers for compressible liquids. *International Journal for Numerical Methods in Fluids*, 26:395–418, 1998.
- [30] W.-W. Kim and S. Menon. A new in-compressible solver for large-eddy simulations. *International Journal of Numerical Fluid Mechanics*, 31:983–1017, 1999.
- [31] W.-W. Kim and S. Menon. Numerical modeling of turbulent premixed flames in the thin-reaction-zones regime. *Combustion Science and Technology*, 160:119–150, 2000.
- [32] W.-W. Kim, S. Menon, and H. C. Mongia. Large eddy simulations of a gas turbine combustor flow. *Combustion Science and Technology*, 143:25–62, 1999.
- [33] M. Latini, O. Schilling, and W. S. Don. Effects of weno flux reconstruction order and spatial resolution on reshocked two-dimensional richtmyer-meshkov instability. *Journal of Computational Physics*, 221:805–836, 2007.
- [34] S. Lee, S. K. Lele, and P. Moin. Direct numerical simulation of isotropic turbulence interacting with a weak shock wave. *Journal of Fluid Mechanics*, 251:533–562, 1993.
- [35] S. Lee, S. K. Lele, and P. Moin. Interaction of isotropic turbulence with shock waves: Effect of shock strength. *Journal of Fluid Mechanics*, 340:225–247, 1997.
- [36] D. K. Lilly. A proposed modification of the germano subgrid-scale closure method. *Physics of Fluids A*, 4(3):633–635, 1992.
- [37] R. Liska and B. Wendroff. Comparison of several difference schemes on 1d and 2d test problems for the euler equations. *SIAM J. Sci. Comput.*, 28(3):995–1017, 2003.
- [38] S. Liu, C. Meneveau, and J. Katz. On the properties of similarity subgrid-scale models as deduced from measurements in a turbulent jet. *Journal of Fluid Mechanics*, 275:83–119, 1994.
- [39] R. Löhner. Finite elements in CFD: what lies ahead. *International Journal for Numerical Methods in Engineering*, 24:1741–1756, 1987.
- [40] K. Mahesh, S. K. Lele, and P. Moin. The influence of entropy fluctuations on the interaction of turbulence with a shock wave. *Journal of Fluid Mechanics*, 334:353–379, 1997.

- [41] S. Menon and N. Patel. Subgrid combustion modeling for les of spray combustion in large-scale combustors. *AIAA Journal*, 46:709–723, 2006.
- [42] C. C. Nelson and S. Menon. Unsteady simulations of compressible spatial mixing layers. *AIAA-98-0786*, 1998.
- [43] E. Oran, J. W. Weber Jr., E. I. Stefaniw, M. H. Lefebvre, and J. D. Anderson Jr. A numerical study of a two-dimensional $h_2 - o_2 - ar$ detonation using a detailed chemical reaction model. *Combustion and Flame*, 113:17–163, 1998.
- [44] E. S. Oran. Shock-driven nonequilibrium turbulence and high-speed deflagrations. *AIAA 2006-1524, 44th AIAA Aerospace Sciences Meeting and Exhibit*, 2005.
- [45] J. J. Quirk. An alternative to unstructured grids for computing gas dynamics flows around arbitrarily complex two-dimensional bodies. *Computer and Fluids*, 23:125–142, 1994.
- [46] J. J. Quirk. A contribution to the great riemann solver debate. *International Journal for Numerical Methods in Fluids*, 18:555–574, 1994.
- [47] J. R. Ristorcelli. A pseudo-sound constitutive relationship for the dilatational covariances in compressible turbulence. *Journal of Fluid Mechanics*, 347:37–70, 1997.
- [48] S. Sarkar. The pressure-dilatation correlation in compressible flows. *Physics of Fluids A*, 4(12):2674–2682, 1992.
- [49] O. Schilling, L. Marco, and W. S. Don. Physics of reshock and mixing in single-modee richtmyer-meshkov instability. *Physics Review E*, 76(026319), 2007.
- [50] Y. R. Shau and D. S. Dolling. Exploratory study of turbulent structure of a compressible shear layer using fluctuating pitot pressure measurements. *Experiments in Fluids*, 12:293–306, 1992.
- [51] C.-W. Shu and S. Osher. Efficient implementation of essentially non-oscillatory shock-capturing schemes. *Journal of Computational Physics*, 83:32, 1989.
- [52] E. F. Toro. *Riemann Solvers and Numerical Methods for Fluid Dynamics - A Practical Introduction*. Addison-Wesley Publishing Company, Inc., 1999.
- [53] E. F. Toro, M. Spruce, and W. Speares. Restoration of the contact surface in the HLL riemann solver. *Shock Waves*, 4:25–34, 1994.
- [54] B. Van Leer. Towards the ultimate conservative difference scheme v. a second order sequel to godunov’s method. *Journal of Computational Physics*, 32:101, 1979.
- [55] M. Vetter and B. Sturtevant. Experiments on the richtmyer-meshkov instability. *Shock Wave*, 4:247–252, 1995.

- [56] B. Vreman, B. Geurts, and H. Kuerten. Realizability conditions for the turbulent stress tensor in large-eddy simulations. *Journal of Fluid Mechanics*, 276:351–362, 1994.
- [57] N. J. Zabusky. Vortex paradigm for accelerated inhomogeneous flows: Visiometrics for the rayleigh-taylor and richtmyer-meshkov environments. *Annu. Rev, Fluid Mech*, 31:495–536, 1999.
- [58] O. Zeman. Dilatational dissipation: the concept and application in modeling compressible mixing layers. *Physics of Fluids A*, 2(2):178–188, 1990.
- [59] Y. Zhou. A scaling analysis of turbulent flows driven by rayleigh-taylor and richtmyer-meshkov instabilities. *Physics of Fluids*, 13(10), 2001.
- [60] Y. Zhou, H. F. Robey, and A. C. Buckingham. Onset of turbulence in accelerated high-reynolds-number flow. *Physics Review E*, 67(056305), 2003.

APPENDIX A

HLLE AND HLLC RIEMANN SOLVERS

A brief description of the *HLL* Riemann solver family is given hereafter. The HLL approximate Riemann solvers have first been developed by Harten, Lax and van Leer ([27]), by expressing a hyperbolic system of conservation laws in integrand form. From an initial interface separating two constant states, it is assumed that N waves can be formed from the characteristics evolution of the system, separating $N + 1$ constant-properties regions. The knowledge of the jump relation through the waves and the wave-speeds can be used to obtain a closed form expression for the intermediate states, and the associated fluxes. Harten [27] carried out a full derivation for a 2 – waves problem, leaving the wavespeeds as sole unknowns to the solver, and have given a mathematical description for the 3-waves problem.

The 2-waves formulation for the resolution of the Euler equations (with wavespeeds expressions given by [18, 19], thus called *HLLE*) has been proven robust and adequate for shocks and rarefactions, but appears to be very dissipative for contact discontinuities. In another study, a correction to the derivation of this solver was proposed ([53]), in order to *add* the missing contact wave (thus, called *HLLC*), whose wavespeed was estimated by an approximation of the particle velocity in the intermediate region. The formulation is closed by expressing the jump conditions across all wave obtained from the exact Riemann solver for the Euler equations. This formulation was further studied by Batten *et al* [3], where the averaged intermediate state was related to the HLLE evaluation, thus leading to an easy, but yet robust, 3-waves Riemann solver. It should be noted that this 3-waves solver does not follow the original work of Harten *et al*, but rather modifies the 2-wave system by introducing the intermediate wave's speed from the 2-wave solver as a correction. The solver does not reduce to a single-wave problem in the physical limit of an isolated discontinuity. It is, however, found robust and yet accurate for the resolution of hydrodynamics problem, and remains very inexpensive compared to other approximate Riemann solvers.

The Riemann solver developed for this study uses a combination of both solvers in order to reduce the instabilities associated to contact-resolving solvers. The simple 2-waves HLL will be described hereafter. The wave-speeds estimates for the HLLE approach, and the modifications that lead to the HLLC solver are also described.

A.1 The 2-waves HLL Riemann Solver

This approximate Riemann solver starts with the assumption that an initial discontinuity gives rise to 2 waves, a left-moving wave (of Eulerian speed S_l), and a right-moving counterpart (of Eulerian speed S_r). A typical (x,t) diagram for a subsonic case is given in Fig. A.1. The integral form of the Euler equations (see, *eg*,

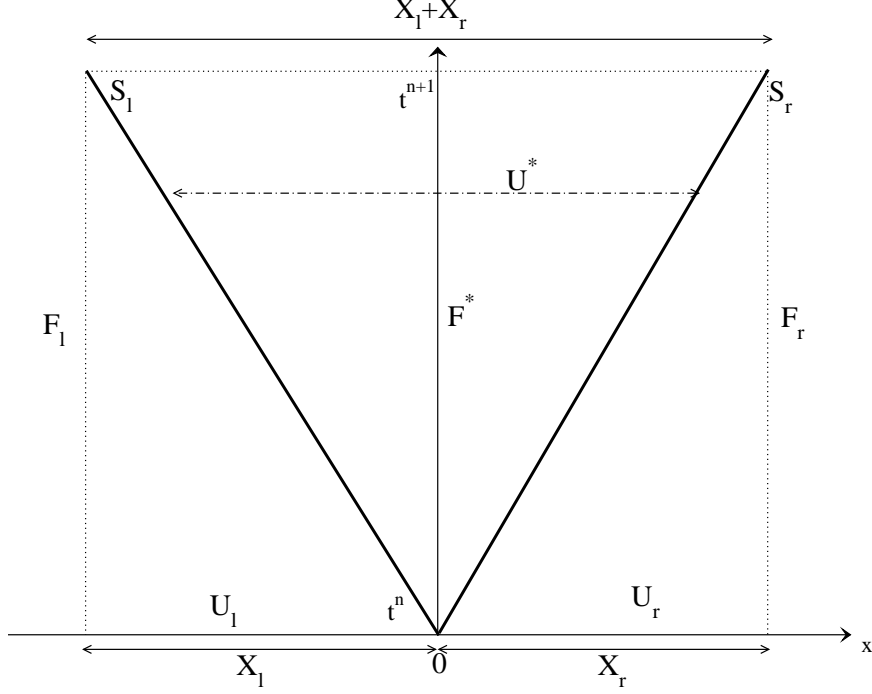


Figure A.1: Two characteristic waves, and their characteristic wavespeeds.

[52]), reads:

$$\oint [U dx - F(U) dt] = 0 \quad (\text{A.1})$$

where, noting $q = \vec{V} \cdot \vec{n} = un_x + vn_y + wn_z$ the interface normal velocity amplitude, U and $F(U)$ are given by:

$$U = \begin{bmatrix} \rho \\ \rho u \\ \rho v \\ \rho w \\ \rho E \\ \rho k^{sgs} \\ \rho Y_k \end{bmatrix}, \quad F = \begin{bmatrix} \rho q \\ \rho u q + P n_x \\ \rho v q + P n_y \\ \rho w q + P n_z \\ (\rho E + P) q \\ \rho k^{sgs} q \\ \rho Y_k q \end{bmatrix} \quad (\text{A.2})$$

Let T be the local time step, $T = t^{n+1} - t^n > 0$. Note that, in all cases, $S_l < S_r$. Let us first treat the case where $S_l > 0$, which corresponds to a supersonic flow from left to right. The S_l wave would lie on the right of the interface, and the flux at $x = 0$, F^* , is then obviously given by $F(U_l)$. Similarly, if $S_r < 0$, the flow is supersonic, from right to left, and F^* is given by $F(U_r)$.

Now, let us examine the case where $S_l \leq 0 \leq S_r$. The lengths X_l, X_r can then be expressed as $X_l = -TS_l$ and $X_r = TS_r$. Expressing the integral form of the Euler

equations on the system in Fig. A.1 gives:

$$\begin{aligned} \int_0^{-X_l} U(x, 0) dx - \int_0^T F(U(X_l, t)) dt + \int_{-X_l}^{X_r} U(x, T) dx \\ - \int_T^0 F(U(X_r, t)) dt + \int_{X_r}^0 U(x, 0) dx = 0 \end{aligned} \quad (\text{A.3})$$

Assuming piecewise constant variables, and hence, piecewise constant fluxes, the previous relation can be re-written as:

$$\begin{aligned} U_l \cdot (S_l T) - F_l \cdot (T) \\ + U^* \cdot ((S_r - S_l) T) - F_r \cdot (-T) + U_r \cdot (-S_r T) = 0 \end{aligned} \quad (\text{A.4})$$

relation that, after re-arrangement, leads to:

$$U^* = \frac{F_l - S_l U_l - (F_r - S_r U_r)}{S_r - S_l} \quad (\text{A.5})$$

This shows that once (U_l, U_r) is known from the reconstruction procedure, and once the wavespeeds (S_l, S_r) are estimated, the variables in the \star -region are fully defined.

The integral relation applied across a given k -wave, $k = (l, r)$, results in the Rankine-Hugoniot relations that read:

$$\begin{aligned} F^* &= F_l + S_l (U^* - U_l) \\ F^* &= F_r + S_r (U^* - U_r) \end{aligned} \quad (\text{A.6})$$

From these 2 relations, one can eliminate U^* in order to determine F^* as:

$$F^* = \frac{S_r F_l - S_l F_r + S_l S_r (U_r - U_l)}{S_r - S_l} \quad (\text{A.7})$$

Thus, the flux evaluated at the $i + 1/2$ interface from the 2-waves HLL Riemann solver reads:

$$F_{i+1/2}^{HLL E} = \begin{cases} F_l & \text{if } 0 \leq S_l \\ F^* & \text{if } S_l \leq 0 \leq S_r \\ F_r & \text{if } S_r \leq 0 \end{cases} \quad (\text{A.8})$$

Once an evaluation of the wavespeeds (S_l, S_r) is provided, the HLL Riemann solver is fully defined. A few wavespeeds estimates can be found in the literature ([13, 18, 19, 52]), leading to schemes of different robustness and dissipation. In the present development, the wavespeeds are estimated following the work of Einfeldt (the HLL solver with Einfeldt wave-speeds is referred to as HLLE), as:

$$S_l = \min [q_l - c_l, \tilde{q} - \tilde{c}] \quad S_r = \max [q_r + c_r, \tilde{q} + \tilde{c}] \quad (\text{A.9})$$

where \tilde{U} here refers to the Roe-averaged variable U , and c is the local speed of sound.

This solver has proven to be robust and accurate for hypersonic calculations and shock capturing purposes. Its assumption of double waves is however limiting, and the consequent numerical smearing of contact discontinuities, shear waves, etc... makes it unsuitable for viscous, turbulent calculations. An extension of this scheme has been developed and presented by [53], where the middle wave in the Riemann problem is taken into account in the derivation of the fluxes. This extended Riemann solver is named HLLC (C standing for Contact), and its derivation is given in the next section.

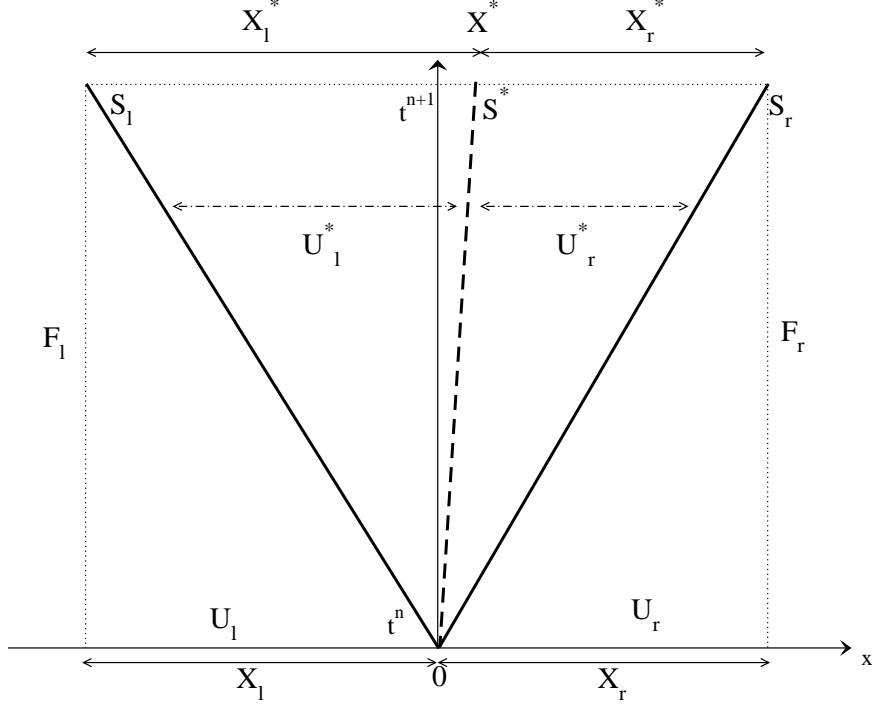


Figure A.2: Three characteristic waves, and their characteristic wavespeeds.

A.2 Restoration of the middle wave - the HLLC Riemann Solver

This approximate Riemann solver starts with the assumption that, at a given interface separating two states in a *shock – tube*-like configuration, the time evolution of a system governed by the Euler equations gives rise to three waves, of speed S_l for the left moving wave, S_r for the right moving wave, and S^* for the contact wave. It is then assumed that these waves can be represented as infinitely thin discontinuities, separating constant states of the fluid. S_l separates U_l from U_l^* , S^* is the interface between U_l^* and U_r^* , while S_r separates U_r^* from U_r . This assumption of thin interfaces is justified for both shocks and contact discontinuities, and is an approximation in the case of rarefactions. A typical representation of a subsonic system is shown in Fig. A.2.

Let T be the local time step, $T = t^{n+1} - t^n > 0$. Note that, in all cases, $S_l < S^* < S_r$. Similarly to the *HLL* solver, the case of a supersonic flow from left to right, where $S_l > 0$, leads to a flux at $x = 0$ given by $F(U_l)$. Again, if $S_r < 0$, the flux is given by $F(U_r)$. Now, let us examine the case when $S_l \leq 0 \leq S_r$. The lengths X_l and X_r can then be expressed as $X_l = -TS_l$ and $X_r = TS_r$ respectively, and similarly, $X_l^* = T(S^* - S_l)$, $X_r^* = T(S_r - S^*)$. The Euler equations in integral form, Eqn. A.1,

can be applied to the system represented in Fig. A.2, leading to the relation:

$$\begin{aligned} & \int_0^{-X_l} U(x, 0) dx - \int_0^T F(U(X_l, t)) dt + \int_{-X_l}^{X^*} U(x, T) dx \\ & + \int_{X^*}^{X_r} U(x, T) dx - \int_T^0 F(U(X_r, t)) dt + \int_{X_r}^0 U(x, 0) dx = 0 \end{aligned} \quad (\text{A.10})$$

With the same assumptions of piecewise constant variables and piecewise constant fluxes as in the derivation of the *HLL* solver, the previous relation can be re-written as:

$$\begin{aligned} & U_l \cdot (S_l T) - F_l \cdot (T) + U_l^* \cdot ((S^* - S_l) T) \\ & + U_r^* \cdot ((S_r - S^*) T) - F_r \cdot (-T) + U_r \cdot (-S_r T) = 0 \end{aligned} \quad (\text{A.11})$$

relation that, after re-arrangement, leads to:

$$(S^* - S_l) U_l^* + (S_r - S^*) U_r^* = F_l - S_l U_l - (F_r - S_r U_r) \quad (\text{A.12})$$

This relation relates the left and right \star -variables together, and is often called the consistency condition. Note that assuming a unique \star -state, so that $U_l^* = U_r^*$ recovers the Consistency Condition of the *HLL* solver, Eqn. A.5.

The integral applied around a control volume surrounding a given k -wave leads to:

$$U_k \cdot (S_k T) - F_k \cdot (T) - U_k^* \cdot (-S_k T) + F_k^* \cdot (T) = 0 \quad (\text{A.13})$$

so that the corresponding Rankine-Hugoniot relations across the k -wave, $k = (l, r)$, are recovered, and reads:

$$\begin{aligned} F_l^* &= F_l + S_l (U_l^* - U_l) \\ F_r^* &= F_r + S_r (U_r^* - U_r) \end{aligned} \quad (\text{A.14})$$

Identically, the Rankine-Hugoniot relation across the \star -wave reads:

$$F_l^* = F_r^* + S^* (U_l^* - U_r^*) \quad (\text{A.15})$$

The relations A.12, A.14 and A.15 give 4 relations for 4 unknowns (F_l^* , F_r^* , U_l^* , and U_r^*). It is however straightforward to show that they are not linearly independent. An assumption has to be made on the intermediate states in order to solve this system of equations.

Toro *et al* [53] closed the relation by assuming that the intermediate wave had the same properties as a contact discontinuity. Its propagation speed is then assumed identical to the convective velocity in the \star -region, and this wave retains the initial discontinuity in the passive scalar field. This also implies that both convective velocities and pressures have to match across the interface. Mathematically, those assumption are expressed by:

$$\begin{aligned} (\vec{V}_l^* \cdot \vec{n} = q_l^*) &= (\vec{V}_r^* \cdot \vec{n} = q_r^*) = S^* \\ P_l^* &= P_r^* \\ \phi_l^* &= \phi_l, \quad \phi_r^* = \phi_r \end{aligned} \quad (\text{A.16})$$

where ϕ is any passive scalar advected by the fluid ($\phi = k^{sgs}, Y_k, \dots$). Note that one special case of passive scalar in the present approach is the component of the velocity

transverse to the interface, $\phi_k = \vec{V}_k - (\vec{V}_k \cdot \vec{n}) \vec{n} = \vec{V}_k - S^* \vec{n}$, $k = (l, r)$. As mentioned in Toro [52], all of these conditions are exactly satisfied by a contact discontinuity computed from an exact Riemann solver.

With these assumptions, one can re-write the four first elements of the vectorial equation expressed in Eqn. A.12, as:

$$\begin{aligned}
 (S^* - S_l) \underbrace{\begin{bmatrix} \rho_l^* \\ \rho_l^* u_l^* \\ \rho_l^* v_l^* \\ \rho_l^* w_l^* \end{bmatrix}}_{U_l^*} + (S_r - S^*) \underbrace{\begin{bmatrix} \rho_r^* \\ \rho_r^* u_r^* \\ \rho_r^* v_r^* \\ \rho_r^* w_r^* \end{bmatrix}}_{U_r^*} &= S_r \underbrace{\begin{bmatrix} \rho_r \\ \rho_r u_r \\ \rho_r v_r \\ \rho_r w_r \end{bmatrix}}_{U_r} - S_l \underbrace{\begin{bmatrix} \rho_l \\ \rho_l u_l \\ \rho_l v_l \\ \rho_l w_l \end{bmatrix}}_{U_l} + \\
 &\underbrace{\begin{bmatrix} \rho_l q_l \\ \rho_l q_l u_l + P_l n_x \\ \rho_l q_l v_l + P_l n_y \\ \rho_l q_l w_l + P_l n_z \end{bmatrix}}_{F_l} - \underbrace{\begin{bmatrix} \rho_r q_r \\ \rho_r q_r u_r + P_r n_x \\ \rho_r q_r v_r + P_r n_y \\ \rho_r q_r w_r + P_r n_z \end{bmatrix}}_{F_r}
 \end{aligned} \tag{A.17}$$

By assumption, $q_k^* = S^*$ for both $k = l/r$. Projecting the vectorial momentum equation on the directional unit vector gives, along with the first relation, the following set of two equations:

$$\begin{aligned}
 \rho_l^* (S^* - S_l) + \rho_r^* (S_r - S^*) &= \rho_r (S_r - q_r) - \rho_l (S_l - q_l) \\
 \underbrace{\left[\rho_l^* (S^* - S_l) + \rho_r^* (S_r - S^*) \right]}_{\text{bracketed term}} S^* &= P_l - P_r + \rho_r q_r (S_r - q_r) - \rho_l q_l (S_l - q_l)
 \end{aligned} \tag{A.18}$$

Replacing the under-braced term in the last equation by the right-hand side of the first equation above leads to:

$$S^* = \frac{P_r - P_l + \rho_l q_l (S_l - q_l) - \rho_r q_r (S_r - q_r)}{\rho_l (S_l - q_l) - \rho_r (S_r - q_r)} \tag{A.19}$$

It is then possible to manipulate Eqn. A.14 and get the expressions for all \star -variables. One can write the first four relations, for continuity and momentum:

$$\underbrace{\begin{bmatrix} \rho_k^* S^* \\ \rho_k^* S^* u_k^* + P_k^* n_x \\ \rho_k^* S^* v_k^* + P_k^* n_y \\ \rho_k^* S^* w_k^* + P_k^* n_z \end{bmatrix}}_{F_k^*} = \underbrace{\begin{bmatrix} \rho_k q_k \\ \rho_k q_k u_k + P_k n_x \\ \rho_k q_k v_k + P_k n_y \\ \rho_k q_k w_k + P_k n_z \end{bmatrix}}_{F_k} + S_k \left(\underbrace{\begin{bmatrix} \rho_k^* \\ \rho_k^* u_k^* \\ \rho_k^* v_k^* \\ \rho_k^* w_k^* \end{bmatrix}}_{U_k^*} - \underbrace{\begin{bmatrix} \rho_k \\ \rho_k u_k \\ \rho_k v_k \\ \rho_k w_k \end{bmatrix}}_{U_k} \right) \tag{A.20}$$

the first relation leads directly to an expression for the density in the *star* region:

$$\rho_k^* = \rho_k \frac{S_k - q_k}{S_k - S^*} \tag{A.21}$$

Again, multiplying the second relation by n_x , the third by n_y and the last by n_z , adding those three relations, and using the expression for ρ_k^* given in Eqn. A.21 leads directly to:

$$P_k^* = P_k + \rho_k(q_k - S_k)(q_k - S^*) \quad (\text{A.22})$$

Note that the relation expressed in Eqn. A.22 is valid for both $k = (l, r)$, and satisfies $P_l^* = P_r^*$. Let us define β_k , α_k and ω_k as:

$$\begin{aligned} \beta_k &= \frac{S^* - q_k}{S_k - S^*} \\ \alpha_k &= \beta_k + 1 \\ \omega_k &= -\beta_k(q_k - S_k) \end{aligned} \quad (\text{A.23})$$

The state vectors U_k^* can then be expressed as:

$$U_k^* = \alpha U_k + \begin{bmatrix} 0 \\ \rho_k \omega_k n_x \\ \rho_k \omega_k n_y \\ \rho_k \omega_k n_z \\ \frac{P^* S^* - P_k q_k}{(S_k - S^*)} \\ 0 \\ 0 \end{bmatrix} \quad (\text{A.24})$$

With these relations, the evaluation of the wavespeeds provides the description of all states in the Riemann problem under consideration. It is then possible to describe the fluxes at $i + 1/2$ interface. The general expression for these fluxes is given by:

$$F_{i+1/2}^{HLLC} = \begin{cases} F_l & \text{if } 0 \leq S_l \\ F_l^* = F_l + S_l(U_l^* - U_l) & \text{if } S_l \leq 0 \leq S^* \\ F_r^* = F_r + S_r(U_r^* - U_r) & \text{if } S^* \leq 0 \leq S_r \\ F_r & \text{if } S_r \leq 0 \end{cases} \quad (\text{A.25})$$

The HLLC Riemann solver is then fully defined, and only the wavespeeds are needed to close its expression. The estimates used in the HLLE solver are used for the evaluation of S_l and S_r , whereas S^* is defined through relation A.19.